

We are IntechOpen, the world's leading publisher of Open Access books Built by scientists, for scientists

6,900

Open access books available

186,000

International authors and editors

200M

Downloads

154

Countries delivered to

TOP 1%

most cited scientists

12.2%

Contributors from top 500 universities



WEB OF SCIENCE™

Selection of our books indexed in the Book Citation Index
in Web of Science™ Core Collection (BKCI)

Interested in publishing with us?
Contact book.department@intechopen.com

Numbers displayed above are based on latest data collected.

For more information visit www.intechopen.com



Topochemical Conversion of Inorganic–Organic Hybrid Compounds into Low-Dimensional Inorganic Nanostructures with Smart Control in Crystal-Sizes and Shapes

Deliang Chen

*School of Materials Science and Engineering,
Zhengzhou University,
P. R. China*

1. Introduction

Nanomaterials with low-dimensional morphologies, including 0D QDs, 1D nanowires (nanotubes and nanoneedles), and 2D nanoplates (nanosheets and nanodisks), have giant potential applications in catalysts, sensors, and medical treatment. Since the end of the last century, there have developed various methods to synthesize low-dimensional nanocrystals. The well-established synthetic methods mainly include CVD, PVD, Sol-Gel processes, soft/hard templating processes, and mechanical balling, most of which have successfully been used to fabricate various nanomaterials with sophisticate morphologies. But at the same time, we usually find a few insurmountable issues when using these methods to synthesize nanomaterials on a large scale: (1) the poor uniformity in crystal-size and shape, (2) the serious agglomeration of small nanoparticles, (3) the high synthetic costs and low outputs, and so on. These issues restrict the extensive applications of low-dimensional nanomaterials to a large extent.

Exfoliation of layered compounds is a common way to synthesize 2D nanocrystals. Colloid nanosheets of titanate, niobate, MnO_2 , clays, and layered double hydroxides (LDHs) have been synthesized from totally exfoliating their corresponding layered compounds. The nanosheets obtained by such exfoliation processes are usually extremely thin and tend to form hard aggregates easily when the solvents are removed. At the same time, nanosheets can be used as building blocks to construct novel metastable 3D structures through condensation, thermal decomposition, and recrystallization, allowing fine control over their microscopic or macroscopic structural features.

Recently, we have developed a novel strategy to synthesize low-dimensional nanocrystals on the basis of interaction chemistry. The key points of this method lie in two aspects: (1) synthesis of inorganic-organic hybrid precursors with controlled morphologies and shapes, and (2) topochemical conversion of inorganic-organic hybrid precursors to low-dimensional inorganic nanocrystals by removing the organic species. Fig. 1 shows the schematic process of conversion of tungstate-based inorganic-organic hybrid belts to WO_3 nanoplates via an

intermediate product of H_2WO_4 nanoplates. The similar process can be used to synthesize MoO_3 nanoplates. The outstanding advantages of the topochemical process can be described as the followings: (1) The starting materials are easily obtained without captious requirements; (2) The synthetic process is not sensitive to the operation parameters and has high repeatability and stability in product quality; (3) This process is suitable for large-scale and cost-effective synthesis of low-dimensional nanomaterials.

This chapter deals with the synthesis of WO_3 and MoO_3 nanoplates using H_2WO_4 , $H_2W_2O_7$, and $MoO_3 \cdot H_2O$ solid powders as the starting materials.^[1-7] The synthesis of carbides and nitrides of tungsten is also introduced using the as-obtained tungstate-based inorganic-organic hybrid compounds as precursors.^[8,9] The applications of WO_3 and MoO_3 nanoplates in sensors are also introduced.^[6,10,11] The related mechanisms are discussed in some details.^[1-11]

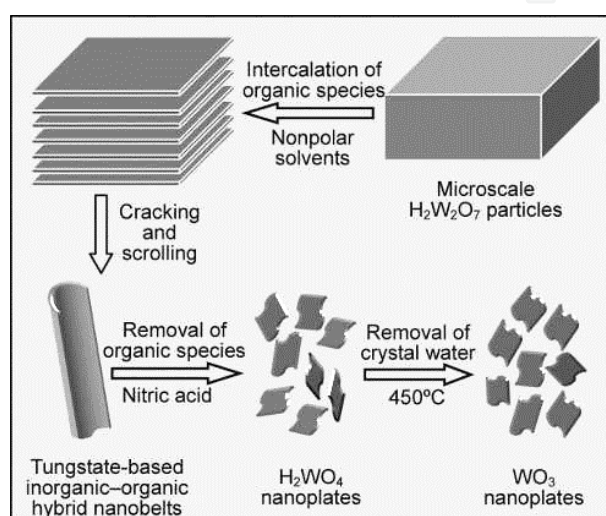


Fig. 1. The schematic representation of the conversion process from microscale $H_2W_2O_7$ particles and tungstate-based inorganic-organic hybrid belts to WO_3 nanoplates via an intermediate product of H_2WO_4 nanoplates. Reprinted with permission from *Small*, 2008, 4(10), 1813-1822. Copyright 2008 Wiley-VCH Verlag GmbH & Co. KGaA.

2. Formation of tungstate-based inorganic-organic hybrid compounds^[1-4]

2.1 Material synthesis and characterization

Tungstate-based inorganic-organic hybrid belts were synthesized through reactions of tungstate acids and alkylamines in a nonpolar solvent at ambient conditions. There were two processes to form tungstate-based inorganic-organic hybrid micro-/nanobelts: one was using $H_2W_2O_7 \cdot xH_2O$ as the host material (i.e., the $H_2W_2O_7 \cdot xH_2O$ process) and the other was using commercial H_2WO_4 as the host material (i.e., the H_2WO_4 process).

For the $H_2W_2O_7 \cdot xH_2O$ process, a stoichiometric mixture of Bi_2O_3 and WO_3 was calcined at 800 °C for 2 days with intermittent grinding to synthesize $Bi_2W_2O_9$ powders. Selective leaching of Bi_2O_2 layers from the as-obtained $Bi_2W_2O_9$ by HCl treatment led to the formation of its protonated phase, $H_2W_2O_7 \cdot xH_2O$. The reactions between $H_2W_2O_7 \cdot xH_2O$ and *n*-alkylamines were carried out at room temperature under an ambient atmosphere. The same procedure was applied for *n*-alkylamines with various alkyl chain lengths ($C_mH_{2m+1}NH_2$, $4 \leq m \leq 14$). The molar ratios of *n*-alkylamine to $H_2W_2O_7 \cdot xH_2O$ were about 5-30, and the volume ratios of heptane to *n*-alkylamine were maintained at about 2-10. Typically, about 0.3 g of

the air-dried $H_2W_2O_7 \cdot xH_2O$ was dispersed in the mixtures of heptane and *n*-alkylamine with magnetic stirring. After reacting for 30 min or 5 days, the products were collected from the suspensions by centrifugation and washed with ethanol. Other solvents were also used as the solvents for the reactions between $H_2W_2O_7 \cdot xH_2O$ and *n*-octylamine under the similar conditions.

For the H_2WO_4 process, 10 g of H_2WO_4 powders was dispersed in a mixture of 0.4 mol of *n*-octylamine and 530 ml of heptane under a constant magnetic stirring at room temperature for 24 h. The molar ratio of *n*-octylamine to H_2WO_4 was 10 and the volume ratio of heptane to *n*-octylamine was 8. After another reaction time of 2 days, the resultant white solids were collected by centrifugation, washed with ethanol, and then dried under a reduced pressure at room temperature for 2 days. The dried sample was tungstate-based inorganic–organic hybrid nanobelts

X-ray diffraction (XRD), scanning electron microscopy (SEM), transmission electron microscopy (TEM), thermogravimetry (TG), CHN analysis and Fourier transform infrared (FT-IR) spectra were used to characterize the microstructures and compositions of the as-obtained hybrid compounds.

2.2 Results and discussion

Fig. 2 shows the typical morphology and microstructure of a tungstate-based inorganic–organic hybrid obtained with a molar ratio of *n*-octylamine to $H_2W_2O_7 \cdot xH_2O$ of about 30 and a volume ratio of heptane to *n*-octylamine of about 2. The low-magnification SEM image (Fig. 2a) indicates that the product possesses a filamentous morphology with lengths of 10–20 μm . A typical FE-SEM image is shown in Fig. 2b. It is clear that the filamentous structures are nanobelts, most of which are scrolled to make nanotubes with apparent diameters of 200–500 nm. The TEM image (Fig. 2c) corroborates that the product obtained exhibits a belt/tubelike morphology. The high-resolution TEM image at point A of Fig. 2c is shown as Fig. 2d, which indicates that the nanobelt/nanotube has a lamellar structure along its length. The thickness of the nanobelt is 20–50 nm. Its XRD pattern suggests that the interlayer distance of the lamellar structure is 2.59(1) nm.

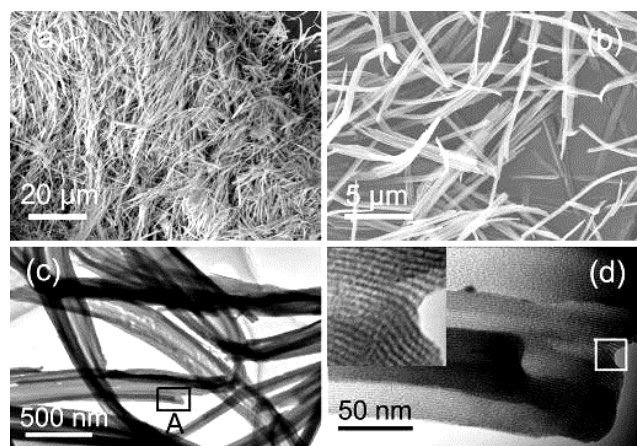


Fig. 2. Typical morphology of the tungstate-based inorganic–organic hybrid accommodating *n*-octylamine with a reaction period of 120 h. Reprinted with permission from *Key Eng. Mater.*, 2007, 352, 85–88. Copyright 2007 Trans Tech Publications Inc.

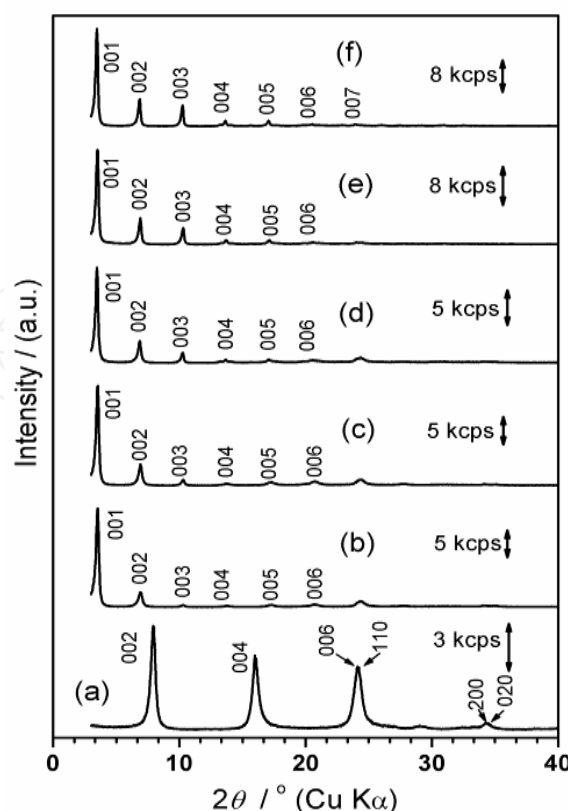


Fig. 3. XRD patterns of the products accommodating *n*-octylamine obtained in a system of heptene/*n*-octylamine/ $\text{H}_2\text{W}_2\text{O}_7 \times \text{H}_2\text{O}$ with various reaction times (*n*-octylamine/ $\text{H}_2\text{W}_2\text{O}_7 \times \text{H}_2\text{O}$ =30): (a) 0 h ($\text{H}_2\text{W}_2\text{O}_7 \times \text{H}_2\text{O}$), (b) 0.5 h, (c) 1 h, (d) 3 h, (e) 5 h and (f) 8 h. Reprinted with permission from *Chem. Mater.*, 2007, 19(7), 1808-1815. Copyright 2007 American Chemical Society.

The XRD patterns of the products obtained after reaction times of 0, 0.5, 1, 3, 5 and 8 h with an *n*-octylamine/ $\text{H}_2\text{W}_2\text{O}_7 \times \text{H}_2\text{O}$ molar ratio of 30 are shown in Figs. 3a-f, respectively. As Fig. 3b shows, a new series of reflections occur in the low 2θ -angle region for the product with a reaction time of 0.5 h. At the same time, the reflections due to the air-dried $\text{H}_2\text{W}_2\text{O}_7 \times \text{H}_2\text{O}$ (Fig. 3a) disappear. The sharp reflections in the low- 2θ range can be indexed to (00*l*) reflections from a highly ordered lamellar structure. The number of identifiable reflections is up to six, but their intensities are very low for the reflections with $l \geq 3$. The interlayer distance estimated from the (00*l*) reflections is 2.570(9) nm. With increases in reaction time, the intensities of the (00*l*) reflections become stronger, especially for the reflections with $l \geq 3$, as shown in Figs. 3c-f. The interlayer distances of the products with reaction times of 1, 3, 5 and 8 h are 2.56(1), 2.58(1), 2.58(1) and 2.595(9) nm, respectively. There is no more obvious change in the XRD pattern when the reaction time is longer than 5 h, even after several days.

The morphologies of the products obtained at various stages are shown in Fig. 4. The host compound of $\text{H}_2\text{W}_2\text{O}_7 \times \text{H}_2\text{O}$ takes on a particle-like morphology with distinct cleavage planes, and its particle size ranges from 5 μm to 20 μm (Fig. 4a). The product with a reaction time of 0.5 h (Fig. 4b) shows parallel cracks. The products obtained with longer reaction times (e.g. 1 h and 2 h) exhibit denser cracks (Figs. 4c and d). The product after a reaction time of 3 h (Fig. 4e) begins to be transformed into one-dimensional nanostructures. At this

stage, the particles and the one-dimensional nanostructures coexist. With the continuation of the reaction to 5 h, most of the particles are transformed into one-dimensional nanostructures, as shown in Fig. 4f. The products obtained with reaction times of 8 and 25 h show similar one-dimensional nanostructures. The FE-SEM (lower left inset of Fig. 4f) and TEM images (Fig. 2c) indicate that the one-dimensional nanostructures are nanobelts or nanotubes with apparent diameters of 200–700 nm and lengths of 5–15 μm . The thicknesses of the nanobelts or the nanotube walls are 20–50 nm.

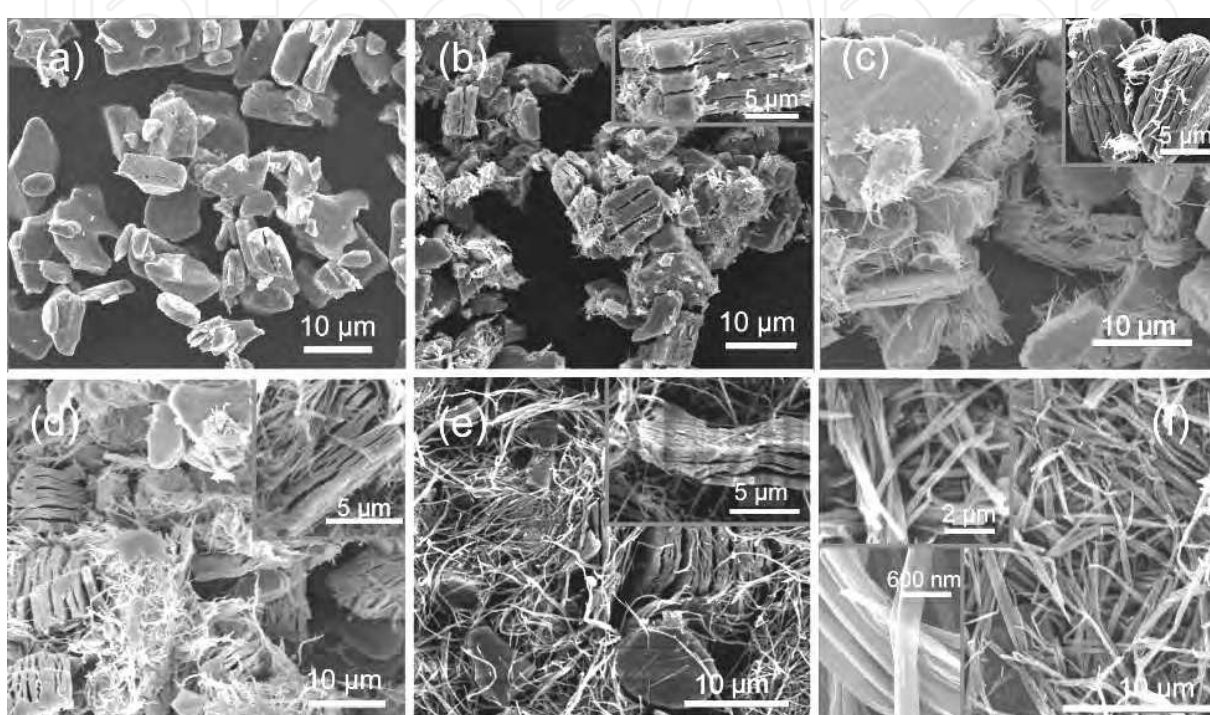


Fig. 4. SEM images of the products accommodating *n*-octylamine after various reaction times (*n*-octylamine/H₂W₂O₇ \times H₂O=30): (a) 0 h (H₂W₂O₇ \times H₂O), (b) 0.5 h, (c) 1 h, (d) 2 h, (e) 3 h and (f) 5 h (the lower left inset is an FE-SEM image of a sample with a reaction period of 120 h). Reprinted with permission from *Chem. Mater.*, 2007, 19(7), 1808-1815. Copyright 2007 American Chemical Society.

The TG analyses indicated that the mass-loss-curve profiles of the products with various reaction times are similar. The mass loss between room temperature and 600 °C increases from 21.8% for the product with a reaction time of 0.5 h to 52.9% for the product with a reaction time of 120 h, as summarized in Table 1. The CHN data are also listed in Table 1. The calculated ratios of C:H:N in moles are (7.8-8.0):(19.2-20.1):1, results very close to the composition (8:19:1 for C:H:N) of *n*-octylamine. The typical FT-IR spectra of the products showed a broad band appearing at around 2110 cm⁻¹, which is due to a combination of the asymmetrical bending vibration and torsional oscillation of the -NH₃⁺ groups interacting with the apical oxygen of the W-O framework, i.e., R-NH₃⁺⋯⋯O-W. When the XRD, TG results and CHN data are taken into account, it can therefore be concluded that the products obtained should be inorganic-organic hybrids with lamellar mesostructures, in which the inorganic W-O layers and the organic species (*n*-octylamine ions) are stacked alternately.

<i>t</i> (h)	<i>M_L</i> (mass %)	C (mass %)	H (mass %)	N (mass %)	<i>R</i>
0.5	21.8	17.68	3.64	2.66	0.563
1	23.7	18.39	3.78	2.73	0.592
3	25.4	19.02	4.03	2.81	0.623
5	36.7	25.52	5.16	3.72	0.973
8	41.3	30.85	6.37	4.51	1.27
25	48.1	35.19	7.31	5.10	1.63
120	52.9	42.48	8.57	6.16	2.16

Table 1. Summary of mass loss (*M_L*) between room temperature and 873 K, data for CHN analysis, and the molar ratio (*R*) of *n*-octylamine taken up to W of the products as a function of reaction time (*t*). Reprinted with permission from *Chem. Mater.*, 2007, 19(7), 1808-1815. Copyright 2007 American Chemical Society.

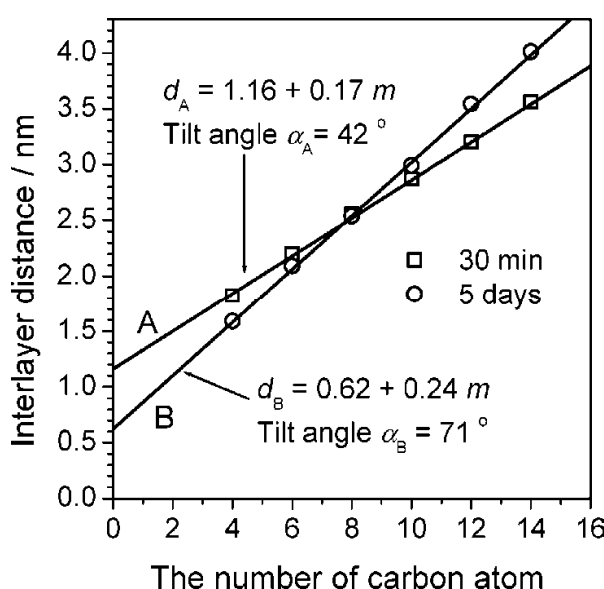


Fig. 5. The plots of the interlayer distance (*d*) versus the *n*-alkyl chain length (*m*, $\text{C}_m\text{H}_{2m+1}\text{NH}_2$) for (A) intermediates with a 30-min reaction time and (B) hybrid nanotubes/nanobelts with a reaction time of 5 days. Reprinted with permission from *Chem. Mater.*, 2007, 19(7), 1808-1815. Copyright 2007 American Chemical Society.

The arrangement of the *n*-alkyl chains and the thickness of the inorganic layers can be evaluated by analyzing the variations in interlayer distance versus the alkyl chain length. The relationship of the interlayer distance (*d*) to the carbon chain length (*n_C*) can generally be described as $d \text{ (nm)} = d_0 + kn_{\text{C}}$, where *k* is the slope and *d₀* is the intercept at *n_C = 0*, and that the increment per $-\text{CH}_2-$ for a fully extended all-trans alkyl chain is 0.127 nm. The slope *k* can therefore give useful information about the arrangement of the *n*-alkyl chains. When *k* \leq 0.127, the arrangement should be a monolayer with a tilt angle *a* ($a = \sin^{-1}(k/0.127)$) or a bilayer with a smaller tilt angle. When $0.127 < k \leq 0.254$, a bilayered arrangement with a tilt angle of $a = \sin^{-1}(k/0.254)$ is usually considered. The intercept *d₀* corresponds to the sum of the thickness of the inorganic layer and the spatial separation due to the amine functional groups.

Fig. 5 shows the plots of the interlayer distance (*d*) versus the *n*-alkyl chain length (*m*, $\text{C}_m\text{H}_{2m+1}\text{NH}_2$) for intermediates with a 30-min reaction time and hybrids with a reaction time

of 5 days. From Fig. 5A, it can be concluded that the *n*-alkyl chains in the intermediates present a bilayered arrangement with a tilt angle $\alpha_A = 42^\circ$, and the thickness of the inorganic layers can be calculated to be 1.00 nm, which is very close to the thickness (0.93 nm) of the double-octahedral W-O layers, suggesting that the double-octahedral W-O layers are preserved in the intermediates obtained in an early stage. Similarly, the slope coefficient of $k_B = 0.24$ suggests that the *n*-alkyl chains in the hybrids take on a bilayered arrangement with a tilt angle of $\alpha_B = \sin^{-1}(0.24/0.254) = 71^\circ$ (Fig. 5A). The thickness of the inorganic layers can be estimated to be 0.39 nm, much lower than the thickness (0.931 nm) of the double-octahedral W-O layers, but very similar to the thickness (0.403 nm) of the single-octahedral W-O layers in H_2WO_4 or $H_2WO_4 \cdot H_2O$.

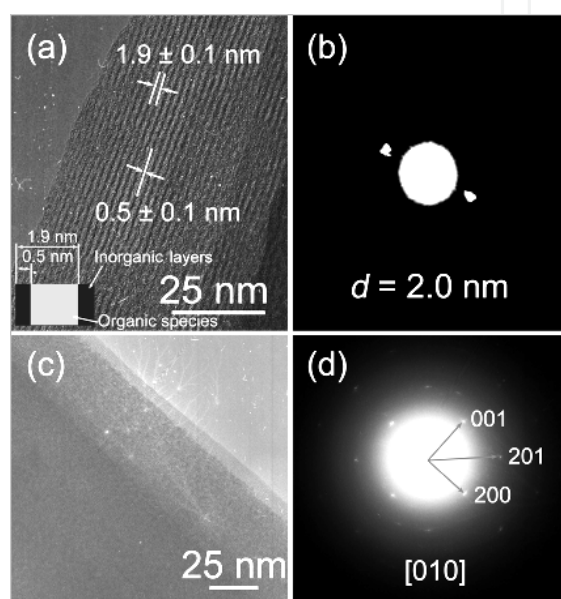


Fig. 6. TEM observation of a tungstate-based organic/inorganic hybrid accommodating *n*-octylamine obtained in heptane with *n*-octylamine/ $H_2W_2O_7 \cdot xH_2O$ = 30: (a) a high-resolution TEM image and (b) an SAED pattern obtained with an incident electron beam parallel to the inorganic layer planes; (c) a high-magnification TEM image and (d) an SAED pattern along the [010] zone axis obtained with an incident electron beam perpendicular to the inorganic layer planes. Reprinted with permission from *Chem. Mater.*, 2007, 19(7), 1808-1815. Copyright 2007 American Chemical Society.

Fig. 6 shows the TEM observations of the inorganic layers in the layered inorganic-organic hybrids with a reaction time of 5 days. Figs. 6a and b show the high-resolution TEM image and the corresponding SAED pattern, respectively, of a case in which the incident electron beam is parallel to the inorganic layers. A black-to-white striped structure with a periodical range interval is observed in Fig. 6a. The black stripes belong to inorganic layers and the white ones are organic species. The interlayer distance and the inorganic thickness can be estimated as 1.9 nm and 0.5 nm, respectively. The one-dimensional diffraction lattices shown in Fig. 6b are typically characteristic of an ordered lamellar structure, the interlayer distance of which is about 2.0 nm calculated according to the equation $d = L\lambda / R$. The interlayer distance (2.0 nm) observed by TEM is slightly smaller than that obtained from the XRD results (about 2.5 nm), probably due to redispersing the hybrid in ethanol to make TEM samples. The directly observed thickness of the inorganic layer is much smaller than

that of the double octahedral W-O layers but close to the single-octahedral W-O layers. The TEM image and its corresponding SAED pattern obtained with the incident electron beam perpendicular to the inorganic layers are shown in Figs. 6c and d, respectively. The discernible two-dimensional diffractional lattices in the SAED pattern can be used to determine the phase of the inorganic layers. As Fig. 6d shows, it can be indexed to the $\text{H}_2\text{WO}_4 \cdot \text{H}_2\text{O}$ phase (JCPDS 18-1420) along the [010] zone axis. The result corroborates that the belt-/tubelike hybrids consist of single-octahedral W-O layers and organic layers.

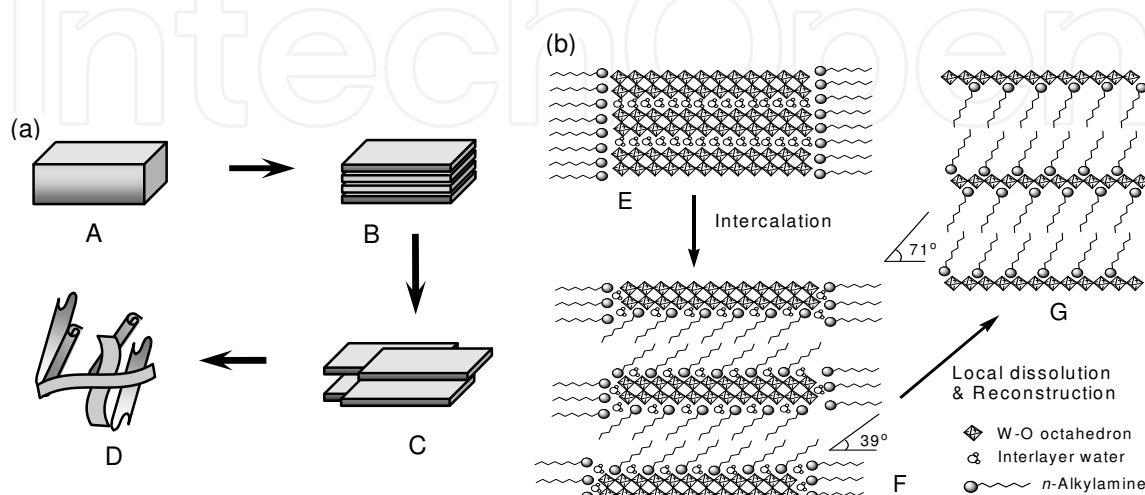


Fig. 7. (a) Macroscopically morphological evolution during the formation of one-dimensional tungstate-based organic/inorganic nanostructures in a system of heptane/*n*-alkylamine/ $\text{H}_2\text{W}_2\text{O}_7 \cdot x\text{H}_2\text{O}$ particles. (b) A formation mechanism of tungstate-based organic/inorganic hybrids with single-octahedral W-O layers from layered $\text{H}_2\text{W}_2\text{O}_7 \cdot x\text{H}_2\text{O}$ solids with double-octahedral W-O layers. Reprinted with permission from *Chem. Mater.*, 2007, 19(7), 1808-1815. Copyright 2007 American Chemical Society.

Fig. 7a illustrates the possible pathway to form belt/tubelike tungstate-based inorganic-organic hybrids. In the very early stages, the microscale $\text{H}_2\text{W}_2\text{O}_7 \cdot x\text{H}_2\text{O}$ particles are gradually cleaved into thin plates, which are aggregates of alternately stacked inorganic-organic layers with thicknesses of 200-800 nm (shown as A → B → C). With the continuation of the reaction, the thin plates are dissolved from their edges to form the final filamentous nanobelts, as shown in C → D. Some of the nanobelts with large widths are spontaneously scrolled into nanotubes to minimize the surface energy. The microstructural development of the inorganic W-O layers and the arrangement of *n*-alkyl chains are illustrated in Fig. 7b. The hydrophilic $\text{H}_2\text{W}_2\text{O}_7 \cdot x\text{H}_2\text{O}$ particles with interlayer water are first dispersed into the nonpolar heptane with the assistance of amphiphilic *n*-alkylamine molecules. The polar heads (-NH₂) of the *n*-alkylamines spread to the surfaces of the inorganic particles, and their alkyl tails spread toward the nonpolar continuous phase, as shown in E. In such reverse-micelle-like media with an excess of *n*-alkylamine, the *n*-alkylamine molecules can directionally diffuse from the nonpolar phase to the interlayer spaces of $\text{H}_2\text{W}_2\text{O}_7 \cdot x\text{H}_2\text{O}$ particles under the interactions of proton transfer. Consequently, normal intercalation occurs easily. The double-octahedral W-O layers are transitorily preserved in the early stage intermediates, constructed by alternately stacking the double-octahedral W-O layers and the bilayer-arranged *n*-alkylammonium ions with a small tilt angle. A typical microstructural model is shown as F. Upon intercalation of *n*-alkylamine, the interlayer water molecules are

released to become “free” water, which then reacts with the surrounding *n*-alkylamine molecules to form highly alkaline solutions in the reverse-micelle-like media. In these space-confined highly alkaline solutions, the double-octahedral W-O layers are therefore dissolved from their edges, and the resultant species subsequently are re-crystallized to form highly ordered lamellar mesostructures with an alternate stacking of single-octahedral W-O layers and bilayer-arranged *n*-alkyl chain arrays with a large tilt angle, as shown in G.

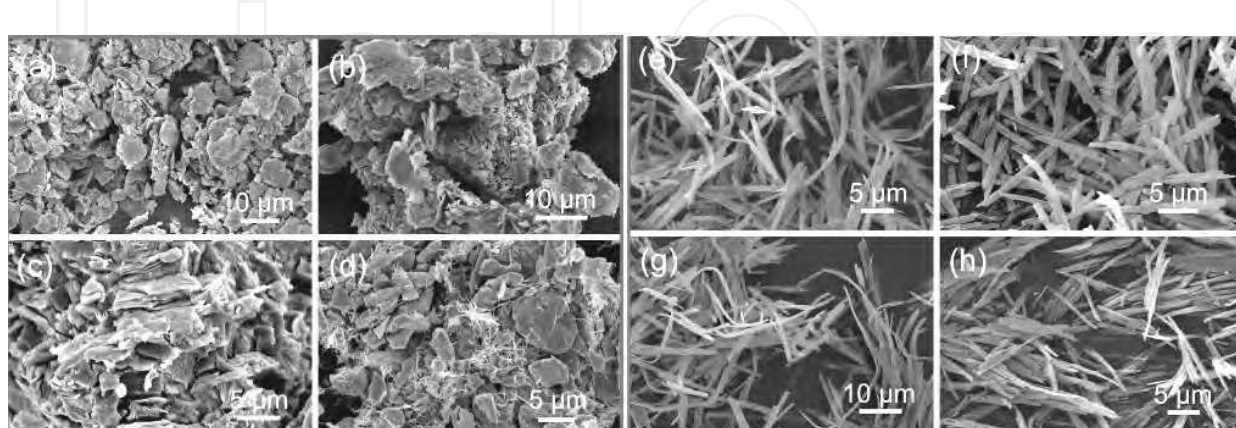


Fig. 8. (a) An SEM image of a hybrid obtained in heptane with an *n*-octylamine-to- $\text{H}_2\text{W}_2\text{O}_7 \times \text{H}_2\text{O}$ ratio of 2; (b-h) SEM images of hybrids obtained in various solvents with an *n*-octylamine-to- $\text{H}_2\text{W}_2\text{O}_7 \times \text{H}_2\text{O}$ ratio of 30: (b) ethanol, (c) tetrahydrofuran, (d) 1-octanol, (e) pentane, (f) decane, (g) 2,2,4-trimethylpentane and (h) cyclohexane. Reprinted with permission from *Chem. Mater.* 2007, 19(7), 1808-1815. Copyright 2007 American Chemical Society.

Fig. 8a displays a typical SEM image of the product obtained after a reaction time of 5 days with a molar *n*-octylamine-to- $\text{H}_2\text{W}_2\text{O}_7 \times \text{H}_2\text{O}$ ratio of 2. Its major morphology is platelike particles with a diameter of about 10 μm , which differs distinctly from the belt/tubelike morphology of the hybrids obtained with high *n*-octylamine: $\text{H}_2\text{W}_2\text{O}_7 \times \text{H}_2\text{O}$ molar ratios (e.g., 30). The XRD pattern showed that the product obtained with an *n*-octylamine: $\text{H}_2\text{W}_2\text{O}_7 \times \text{H}_2\text{O}$ molar ratio of 2 also presented an ordered lamellar structure with an interlayer distance of $d = 2.56(2)$ nm, very close to that of the intermediate obtained after a 30 min reaction, suggesting that the microstructure of the hybrid obtained with a very low molar *n*-octylamine-to- $\text{H}_2\text{W}_2\text{O}_7 \times \text{H}_2\text{O}$ ratio is very similar to that of the intermediate obtained with a short reaction time.

The solvent types also have important influences on the reaction behavior of $\text{H}_2\text{W}_2\text{O}_7 \times \text{H}_2\text{O}$ with *n*-alkylamines. No reaction was observed, or the reactions occurred to a very limited extent, in the solvents of 2-propanol, butanol, and acetone. In the cases of ethanol and THF, no belt/tubelike shapes, but instead platelike ones are observed, as shown in Figs. 8b and c. When 1-octanol is used as the reaction solvent, an ordered lamellar hybrid, with beltlike shapes besides a very small fraction of plates, is obtained (Fig. 8d). With the solvents of nonpolar alkanes, on the other hand, including not only heptane but also other alkanes, such as pentane, decane, 2,2,4-trimethylpentane, and cyclohexane, inorganic-organic hybrids with uniform belt/tubelike morphology are readily obtained, as shown in Figs. 8e-h. Their XRD patterns indicated that all these products obtained with other alkanes possess highly ordered lamellar mesostructures.

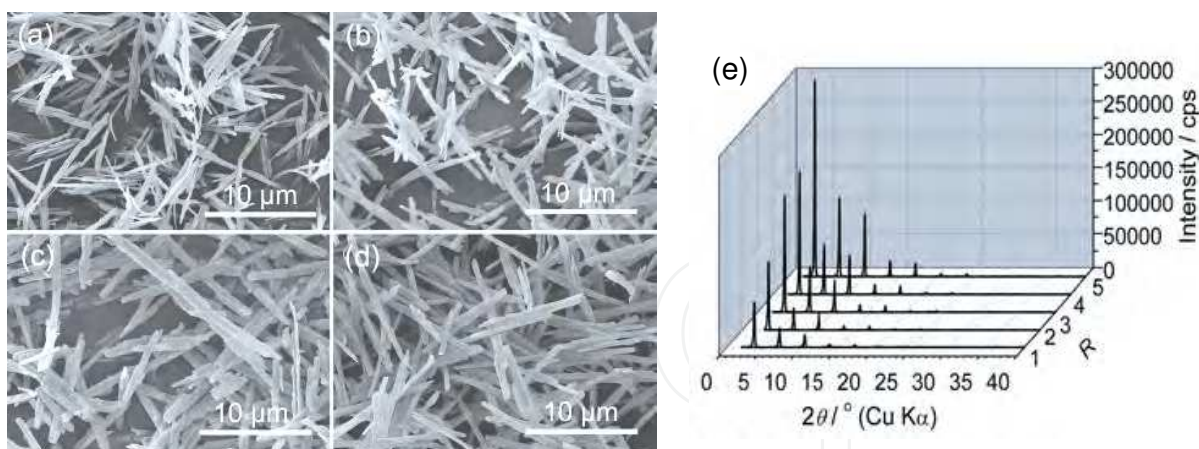


Fig. 9. (a-d) SEM images the products synthesized with various volume ratios (R) of heptane to *n*-octylamine: (a) 1, (b) 3, (c) 4, and (d) 5; (e) XRD patterns of the products synthesized with various volume ratios (R) of heptane to *n*-octylamine. Reprinted with permission from *Key Eng. Mater.*, 2007, 352, 85-88. Copyright 2007 Trans Tech Publications Inc.

The volume ratio of heptane to *n*-octylamine in the reaction system of $\text{H}_2\text{W}_2\text{O}_7 \cdot x\text{H}_2\text{O}/n$ -octylamine/heptane has an obvious effect on the morphology and microstructure of the final products. Figs. 9(a-d) show typical SEM images of products obtained under similar conditions (molar ratio of *n*-octylamine to $\text{H}_2\text{W}_2\text{O}_7 \cdot x\text{H}_2\text{O}$: 30; the reaction time: 120 h; $x \sim 3.5$), except for the volume ratio of heptane to *n*-octylamine, R . As the figure shows, when the R value increases from 1 to 5, the products obtained take on a more uniform belt/tubelike morphology in both diameter and length. The corresponding XRD patterns are shown in Fig. 9e. It can be readily observed that the intensities of the reflections of the products become stronger with increases in the R value from 1 to 5. These results indicate that the degree of the long-range order of the alternate stacking of the *n*-alkyl chains and the inorganic W-O layers in the products obtained in the diluted reaction systems has obviously been enhanced. The enhancement of both the morphology and the microstructure of the products can be considered to be due to a reduced number of collisions among the filamentous structures formed in the dilute reaction systems.



Fig. 10. SEM images of the products synthesized using $\text{H}_2\text{W}_2\text{O}_7 \cdot x\text{H}_2\text{O}$ with various amounts of interlayer water: (a) $x = 4.1$, (b) $x = 2.6$ and (c) $x = 0.85$. Reprinted with permission from *Key Eng. Mater.*, 2007, 352, 85-88. Copyright 2007 Trans Tech Publications Inc.

Fig. 10 shows the SEM images of the products obtained with three kinds of $\text{H}_2\text{W}_2\text{O}_7 \cdot x\text{H}_2\text{O}$ with different amounts of interlayer water: $x = 4.1$, 2.6, and 0.85. All of the products obtained show a very similar belt/tubelike morphology. The rate of the reaction between

$\text{H}_2\text{W}_2\text{O}_7 \cdot x\text{H}_2\text{O}$ and *n*-octylamine could be qualitatively determined based on the time needed for the reaction system to turn from yellow to white. For $x = 4.1$, a white suspension was obtained after a reaction time of about 1 h, whereas for $x = 0.85$, it took more than 10 h for the reaction system to change to a white suspension. When 120 °C-dried $\text{H}_2\text{W}_2\text{O}_7$ ($x = 0$) was used as a precursor to react with *n*-octylamine under similar conditions, there was no obvious change in color, even after a reaction time of 5 days.

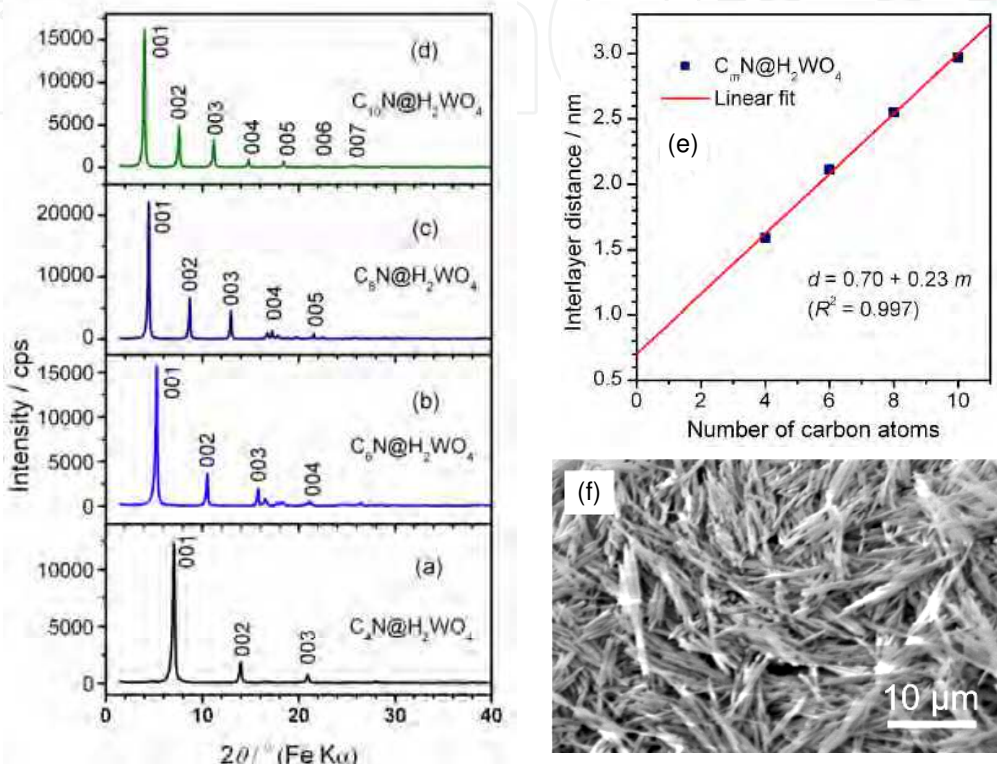


Fig. 11. (a-d) XRD patterns of the tungstate-based hybrid compounds ($\text{C}_m\text{N}@\text{H}_2\text{WO}_4$) obtained via reactions between H_2WO_4 and *n*-alkylamines in heptane: (a) $\text{C}_4\text{N}@\text{H}_2\text{WO}_4$, (b) $\text{C}_6\text{N}@\text{H}_2\text{WO}_4$, (c) $\text{C}_8\text{N}@\text{H}_2\text{WO}_4$, and (d) $\text{C}_{10}\text{N}@\text{H}_2\text{WO}_4$; (e) A plot of the interlayer distances of the $\text{C}_m\text{N}@\text{H}_2\text{WO}_4$ compounds as a function of the carbon numbers of the corresponding *n*-alkylamines; (f) a typical SEM image of the as-obtained $\text{C}_8\text{N}@\text{H}_2\text{WO}_4$ hybrid. Reprinted with permission from *Mater. Chem. Phys.*, 2011, 125(3), 838-845. Copyright 2011 Elsevier.

The reaction behavior of commercially available H_2WO_4 with *n*-alkylamines in reverse-microemulsion-like reaction media, *i.e.*, inorganic particles/*n*-alkylamines/heptane is similar to that of $\text{H}_2\text{W}_2\text{O}_7 \cdot x\text{H}_2\text{O}$ powders. H_2WO_4 powders reacting with *n*-alkylamines at room temperature led to the formation of inorganic-organic hybrid one-dimensional nanobelts, consisting of organic *n*-alkylammonium ions (a bilayered arrangement with a tilt angle of 65°) and inorganic single-octahedral W-O layers, as shown in Fig. 11. The similarity in both compositions and microstructures indicated the reactions of H_2WO_4 and $\text{H}_2\text{W}_2\text{O}_7 \cdot x\text{H}_2\text{O}$ powders with *n*-alkylamines underwent a similar “dissolution-reorganization” process, where the double-octahedral W-O layers from $\text{H}_2\text{W}_2\text{O}_7 \cdot x\text{H}_2\text{O}$ particles were firstly decomposed and the decomposed species were then reorganized into ordered lamellar hybrid nanobelts with inorganic single-octahedral W-O layers, as shown in Fig. 12.

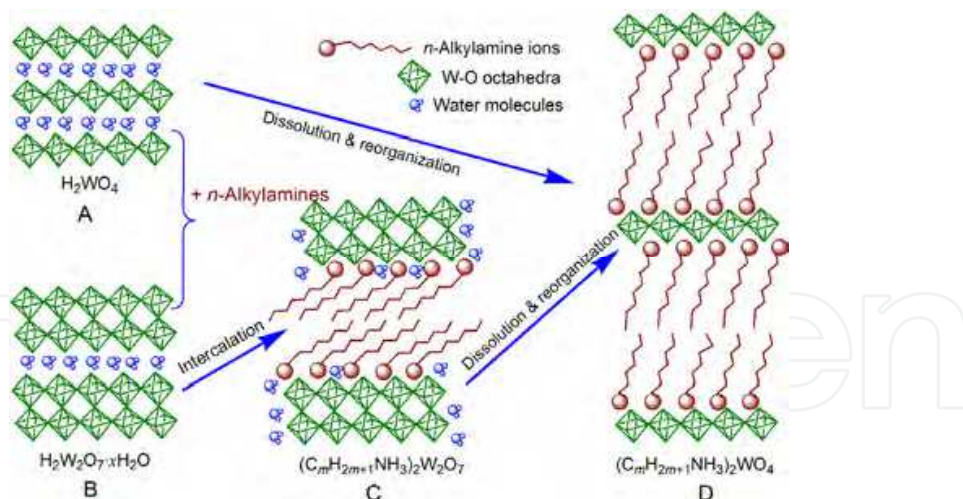


Fig. 12. A schematic of the possible mechanisms for the reactions of $\text{H}_2\text{W}_2\text{O}_7 \cdot x\text{H}_2\text{O}$ and H_2WO_4 with *n*-alkylamines in heptane: (A) H_2WO_4 powders with single-octahedral W–O layers, (B) $\text{H}_2\text{W}_2\text{O}_7 \cdot x\text{H}_2\text{O}$ powders with double-octahedral W–O layers, (C) intermediate hybrids with double-octahedral W–O layers derived by an intercalation reaction, and (D) tungstate-based inorganic-organic hybrids with single-octahedral W–O layers derived by a dissolution–reorganization process. Reprinted with permission from *Mater. Chem. Phys.*, 2011, 125(3), 838–845. Copyright 2011 Elsevier.

3. Topochemical conversion of tungstate-based inorganic-organic hybrid belts to WO_3 nanoplates^[3,5,6]

3.1 Material synthesis and characterization

Typically, 10 g of $\text{H}_2\text{W}_2\text{O}_7 \cdot x\text{H}_2\text{O}$ (*ca.* 20 mmol, $x \approx 1.5$) was dispersed in a mixture of 66 mL of *n*-octylamine (400 mmol) and 330 mL of heptane under a constant magnetic stirring at room temperature. After a reaction time of 72 h, the obtained white solids were collected by centrifugation and washed with ethanol for several times, and then dried under a reduced pressure at room temperature for more than 5 h. The obtained product was tungstate-based inorganic-organic hybrid nanobelts, which were then used as the precursors for the synthesis of $\text{WO}_3 \cdot \text{H}_2\text{O}$ and WO_3 nanoplates. Typically, the obtained hybrid nanobelts (10 g) was dispersed in a mixture of concentrated HNO_3 (60–61 mass %, 200 mL) and distilled H_2O (300 mL) under a stirring condition at room temperature. (*Caution: The reaction releases toxic NO_2 gas, and has to be carried out in a ventilating cabinet.*) A yellow suspension was obtained after a reaction time of more than 2 days. The obtained yellow solids were collected and washed with H_2O and ethanol before air-drying or drying at 120 °C. The air-dried product was $\text{H}_2\text{WO}_4 \cdot \text{H}_2\text{O}$, and the 120 °C-dried product was $\text{WO}_3 \cdot \text{H}_2\text{O}$ nanoplates. The obtained $\text{WO}_3 \cdot \text{H}_2\text{O}$ nanoplates (4.2 g) were calcined at 450 °C for 2 h with a heating rate of 2 °C min⁻¹ in air, and *ca.* 3.9 g of pale yellow WO_3 nanoplates was obtained.

For the preparation of oriented films from tungsten oxide nanoplates, 0.02 g of WO_3 (or $\text{WO}_3 \cdot \text{H}_2\text{O}$) nanoplates was dispersed in 20 mL of ethanol, and the obtained suspension was kept stirring for 3–5 h. 100 µL of the WO_3 (or $\text{WO}_3 \cdot \text{H}_2\text{O}$) suspension was carefully dropped on a pre-washed, horizontally placed XRD glass slice. After the solvent was completely evaporated, another 100 µL of the above suspension was dropped. Such dropping–evaporation process was repeated more than 10 times. The oriented films of WO_3 and $\text{WO}_3 \cdot \text{H}_2\text{O}$ nanoplates supported by XRD glass slices were obtained.

X-ray diffraction (XRD), scanning electron microscopy (SEM), and transmission electron microscopy (TEM) were used to characterize the products. The nitrogen (N_2) adsorption-desorption technique was also used to characterize the as-obtained products.

3.2 Results and discussion

Fig. 13a shows a typical SEM image of the tungstate-based organic–inorganic hybrid precursor used for the synthesis of $WO_3 \cdot H_2O$ nanoplates. The hybrid takes on a quasi-1D beltlike morphology with a half-rolled microstructure (marked with an arrow). Fig. 13b shows a typical TEM image of the pristine inorganic species without washing or drying, obtained by oxidizing the hybrid nanobelts using nitric acid (*ca.* 6 mol/L). One can find that the pristine inorganic species are soft wrinkly belts, with a length of more than 5 μm , a width of *ca.* 1 μm and a thickness of less than 50 nm. The XRD pattern indicated that the air-dried inorganic species were monoclinic $H_2WO_4 \cdot H_2O$ (JCPDS no. 18–1420). Fig. 13c shows the TEM image of a typical 120 °C-dried sample. The product consists of quadrangular nanoplates lying along the Cu grids. Fig. 13d shows a single quadrangular nanoplate, the area of which is *ca.* 350 nm \times 480 nm. Fig. 13e shows its corresponding SAED pattern, indexed to orthorhombic $WO_3 \cdot H_2O$ along the [010] zone axis. The uniform wide ordered diffraction spots indicate that the nanoplate is a whole single crystal. Fig. 13f shows the HRTEM image of the nanoplate. The interplanar distances of *ca.* 0.365 and 0.261 nm can be indexed to (101) (or (10–1)) and (200) crystal planes, respectively.

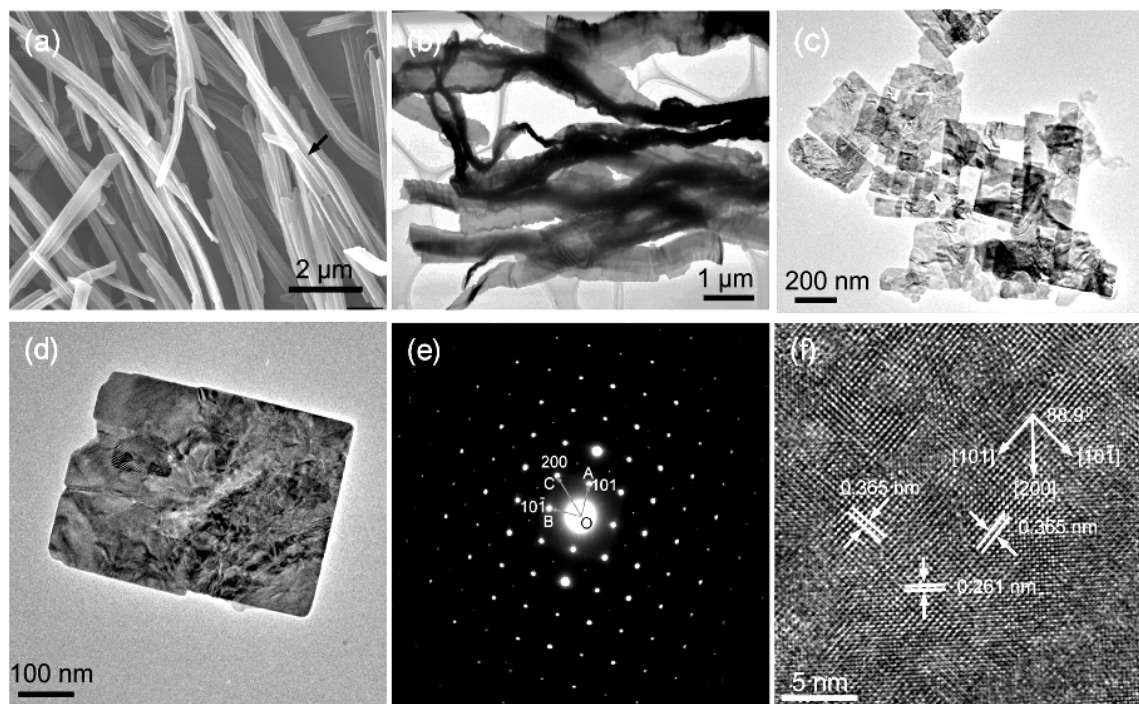


Fig. 13. (a) SEM image of the tungstate-based inorganic–organic hybrid belts; (b) TEM image of $H_2WO_4 \cdot H_2O$ nanobelts without washing or drying treatment; (c) low-magnification TEM image; (d) high-magnification TEM image; (e) SAED pattern along the [010] zone axis; and (f) HRTEM image of H_2WO_4 nanoplates after drying at 120 °C. Reprinted with permission from *Small*, 2008, 4(10), 1813–1822. Copyright 2008 Wiley-VCH Verlag GmbH & Co. KGaA.

Fig. 14 shows the TEM observations of the product derived from $\text{WO}_3 \cdot \text{H}_2\text{O}$ nanoplates by heating them at 450 °C for 2 h with a heating rate of 2 °C min⁻¹. The low-magnification TEM image in Fig. 14a indicates that the calcined product shows a predominant platelike morphology, besides a small fraction of rolled structures (marked with arrows). Fig. 14b shows a single nanoplate with a dimensionality of ca. 230 nm × 420 nm, and Fig. 14c shows its corresponding SAED pattern. The uniform, wide, and well-ordered diffraction spots can be assigned to single-crystal monoclinic WO_3 , along the [001] zone axis. Fig. 14d shows a typical HRTEM image of the edge of the WO_3 nanoplate. The clear lattice structure corroborates that the obtained nanoplate is single-crystal. The interplanar distances are ca. 0.364 and 0.376 nm, assigned to (200) and (020) crystal planes, respectively. Another HRTEM image obtained from the central part of the nanoplate (Fig. 14b) is shown in Fig. 14e. The HRTEM images and SAED pattern indicates that the WO_3 nanoplate derived from the $\text{WO}_3 \cdot \text{H}_2\text{O}$ nanoplate is a whole single crystal. A typical edge dislocation is detected in Fig. 14e (marked with a circle). Fig. 14f shows the EDS spectrum of the WO_3 nanoplate.

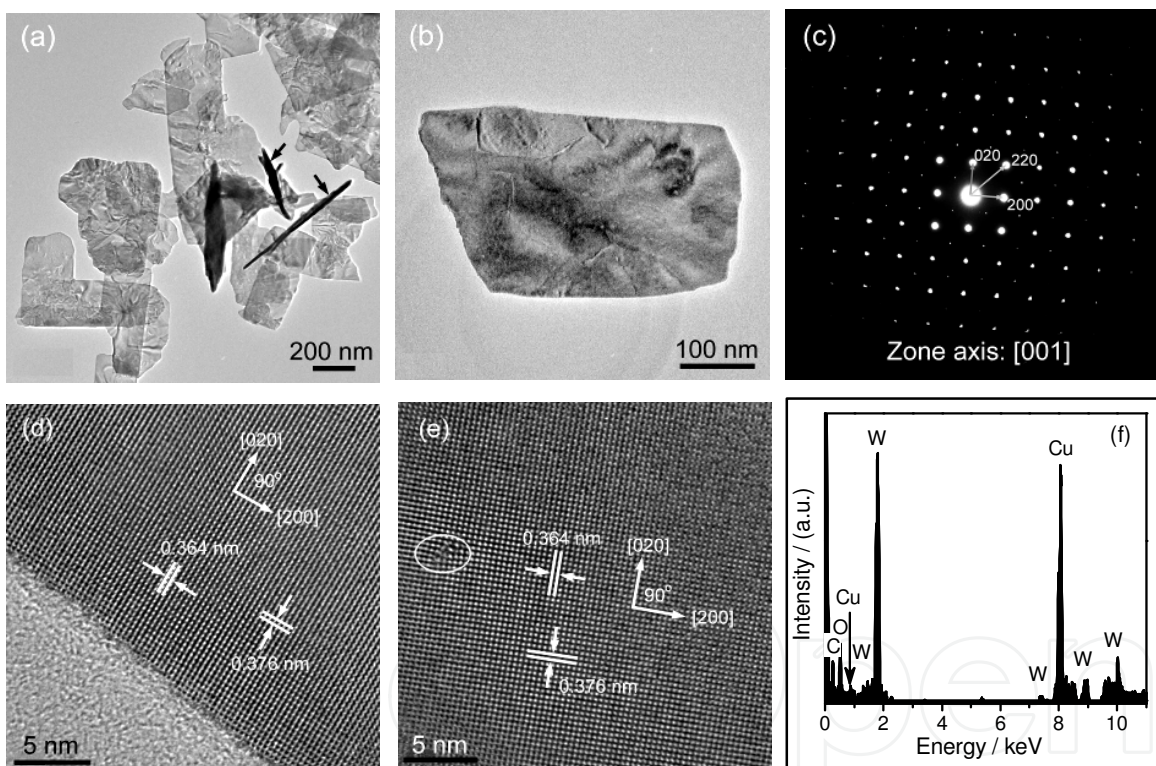


Fig. 14. (a) Low-magnification TEM image; (b) high-magnification image; (c) SAED pattern along the [001] zone axis; (d, e) HRTEM images; and (f) EDS spectrum of the WO_3 nanoplates obtained by calcining H_2WO_4 nanoplates at 450 °C for 2 h with a heating rate of 2 °C min⁻¹. Reprinted with permission from *Small*, 2008, 4(10), 1813-1822. Copyright 2008 Wiley-VCH Verlag GmbH & Co. KGaA.

Fig. 15 shows the SEM images of the obtained $\text{WO}_3 \cdot \text{H}_2\text{O}$ and WO_3 nanocrystals. Both $\text{WO}_3 \cdot \text{H}_2\text{O}$ and WO_3 take on a loose-aggregated-cotton-like morphology. The high-magnification FE-SEM images (Figs. 15b and d) indicate that the cotton-like products consist of thin nanoplates, the thickness of which can be estimated to range from 10 to 30 nm.

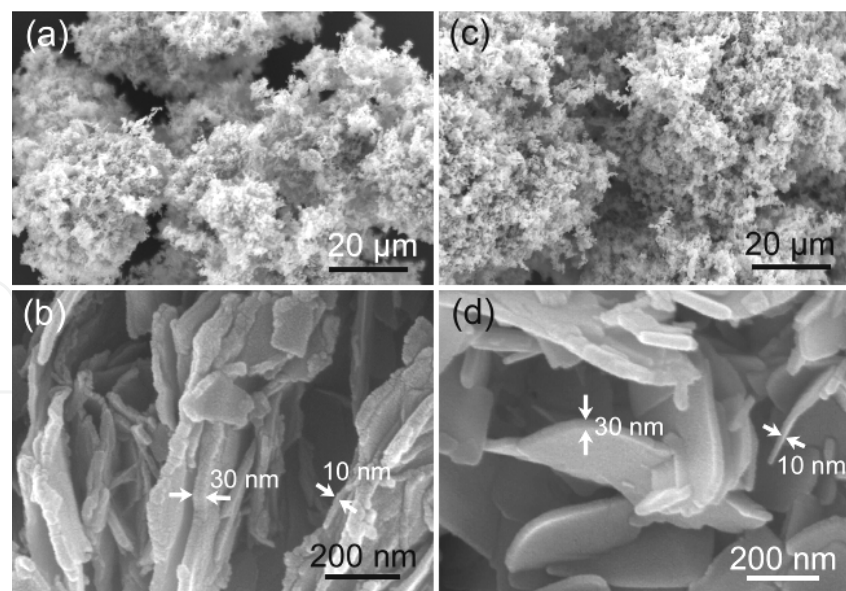


Fig. 15. (a, c) Low-magnification SEM images and (b, d) FE-SEM images of (a, b) the H_2WO_4 nanoplates dried at 120°C and (c, d) WO_3 nanoplates obtained by calcining H_2WO_4 nanoplates at 450°C for 2 h with a heating rate of 2°C min^{-1} . Reprinted with permission from *Small*, 2008, 4(10), 1813–1822. Copyright 2008 Wiley-VCH Verlag GmbH & Co. KGaA.

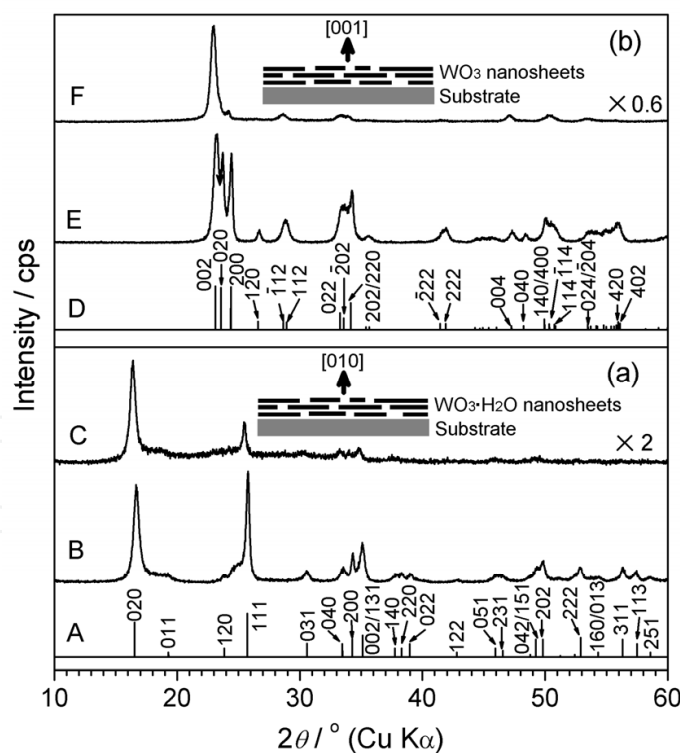


Fig. 16. (a) XRD patterns of (B) the powder sample and (C) the film sample of the obtained $\text{WO}_3 \cdot \text{H}_2\text{O}$ nanoplates (pattern A is the literature data of orthorhombic $\text{WO}_3 \cdot \text{H}_2\text{O}$ (JCPDS no. 43-0679)); (b) XRD patterns of (E) the powder sample and (F) the film sample of the obtained WO_3 nanoplates (pattern D is the literature data of monoclinic WO_3 (JCPDS no. 43-1035)).

Fig. 16 shows the XRD patterns of the obtained $\text{WO}_3 \cdot \text{H}_2\text{O}$ and WO_3 nanoplates in the forms of powders and films. Pattern B is the XRD pattern of the powder sample of $\text{WO}_3 \cdot \text{H}_2\text{O}$ nanoplates. It is very close to the literature data of orthorhombic $\text{WO}_3 \cdot \text{H}_2\text{O}$ phase (pattern A, JCPDS no. 43-0679) not only in the peak positions but also in the intensity ratios of the diffraction peaks. The intensity ratios of (020) to (111) reflections (*i.e.*, I_{020}/I_{111}) of the $\text{WO}_3 \cdot \text{H}_2\text{O}$ powder sample and the literature data are 0.88 and 0.80, respectively. This suggests that $\text{WO}_3 \cdot \text{H}_2\text{O}$ nanoplates in the powder sample are essentially a random orientated aggregate. Pattern C shows a typical XRD result of the film of $\text{WO}_3 \cdot \text{H}_2\text{O}$ nanoplates. One can easily find that the (020) reflection becomes the most intense and the (040) reflection are also detectable, but the other reflections are weakened obviously. The intensity ratio of I_{020}/I_{111} is 2.39, which is twice larger than that (0.88) of its powder sample. Therefore, there is a strong preferred orientation along the [020] direction in the film sample of $\text{WO}_3 \cdot \text{H}_2\text{O}$ nanoplates. From the TEM analysis of $\text{WO}_3 \cdot \text{H}_2\text{O}$ nanoplates, it is determined that the inhibited crystal growth direction of $\text{WO}_3 \cdot \text{H}_2\text{O}$ nanoplates is [010]. Due to the large area-to-thickness ratios, the $\text{WO}_3 \cdot \text{H}_2\text{O}$ nanoplates with an inhibited crystal growth direction of [010] tend to lie along the substrate (inset of Fig. 16a). Thus the (0k0) crystal planes have the largest probability to diffract and the (0k0) reflections have the largest intensities.

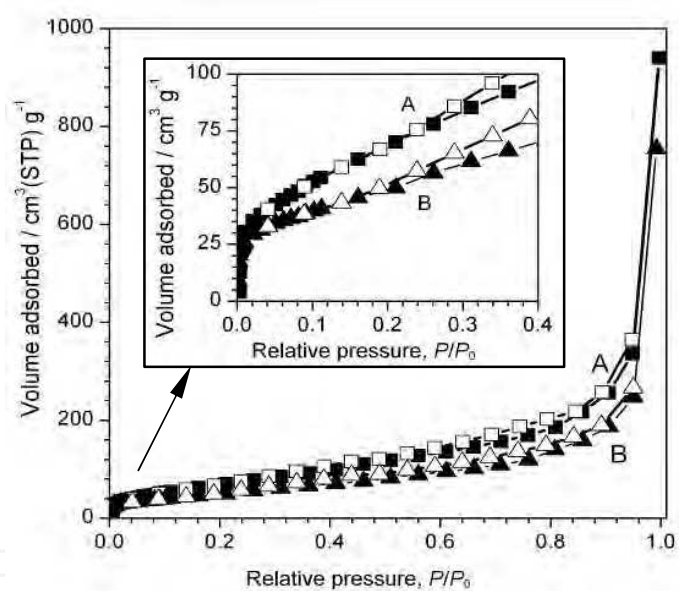


Fig. 17. Nitrogen (N_2) adsorption-desorption isotherms and the corresponding BJH pore-size distribution curves (inset) of the obtained (A) $\text{WO}_3 \cdot \text{H}_2\text{O}$ nanoplates and (B) WO_3 nanoplates (filled: adsorption; open: desorption). Reprinted with permission from *Small*, 2008, 4(10), 1813-1822. Copyright 2008 Wiley-VCH Verlag GmbH & Co. KGaA.

Similarly, the XRD patterns of the powder and film samples of WO_3 nanoplates are shown as patterns E and F in Fig. 16b, respectively. The XRD pattern of the WO_3 nanoplates is consistent with the literature data (pattern D, JCPDS no. 43-1035) of a monoclinic WO_3 phase. The intensity ratios of the (002) to (200) reflection (*i.e.*, I_{002}/I_{200}) of the powder sample of the WO_3 nanoplates and the literature data are 1.21 and 1.01, respectively. The close values in the I_{002}/I_{200} ratios indicate that the powder sample of WO_3 nanoplates shows a very limited preferred orientation and most of the nanoplates aggregate random. But for the

film sample of WO_3 nanoplates, the XRD pattern (pattern F) shows predominant $(00l)$ reflections, and the other reflections disappear or weaken obviously. The I_{002}/I_{200} ratio of the film is 7.94, which is 6.5 times larger than that of its powder sample (1.21). As the proposed schematic model (inset of Fig. 16b) indicates, the WO_3 nanoplates with an inhibited crystal growth direction of $[001]$ and high area-to-thickness ratios prefer lying along the substrate surface to form a $[001]$ -direction orientated film.

Fig. 17 shows the nitrogen (N_2) adsorption–desorption isotherms of the $\text{WO}_3 \cdot \text{H}_2\text{O}$ and WO_3 nanoplates obtained. The $\text{WO}_3 \cdot \text{H}_2\text{O}$ and WO_3 nanoplates show a similar type II isotherm of non-porous solids, with sharp knees (inset of Fig. 17) and without any obvious hystereses. The BET surface areas of the $\text{WO}_3 \cdot \text{H}_2\text{O}$ and WO_3 nanoplates are 257 and 180 $\text{m}^2 \text{ g}^{-1}$, respectively.

4. Formation of MoO_3 nanoplates from molybdate-based inorganic-organic hybrids^[7]

4.1 Material synthesis and characterization

$\text{MoO}_3 \cdot \text{H}_2\text{O}$ powders reacted with *n*-octylamine at room temperature to form molybdate-based inorganic–organic hybrid compounds. Typically, 10.3 mL of *n*-octylamine was firstly mixed with 113.7 mL of ethanol in a conical flask under magnetic stirring, and then 5.0 g of $\text{MoO}_3 \cdot \text{H}_2\text{O}$ powders was dispersed into the above mixture to form a white suspension. The as-obtained suspension was kept stirring for 3 days at room temperature in air, and a white mushy mixture was finally obtained. The white solids were collected by centrifugation, followed by washing with ethanol for three times. The as-obtained solids were then air-dried at room temperature in a reduced pressure for more than 3 days, and 8.1 g of white powders, a molybdate-based inorganic–organic hybrid compound, was obtained. The molar ratios of *n*-octylamine to $\text{MoO}_3 \cdot \text{H}_2\text{O}$ were 2–10. The volume ratios of ethanol to *n*-octylamine were higher than 10.

The as-obtained molybdate-based inorganic–organic hybrid compound was used as the precursor to prepare MoO_3 nanoplates. Typically, 2.0 g of the molybdate-based inorganic–organic hybrid compound was placed in an alumina crucible, which was then put into an electric furnace and kept at 550 °C for 1 h. After naturally cooled down to room temperature, about 1.0 g of gray powders was obtained.

X-ray diffraction (XRD), TEM, HRTEM, TG-DTA, FT-IR, and Raman spectra were used to characterize the molybdate-based inorganic–organic hybrid compounds and the as-obtained MoO_3 nanoplates.

4.2 Results and discussion

Figs. 18a–b show the XRD patterns of the $\text{MoO}_3 \cdot \text{H}_2\text{O}$ and the resultant hybrid compound, respectively. The commercial $\text{MoO}_3 \cdot \text{H}_2\text{O}$ may be a mixture or intermediate phases of molybdic acids with a certain amount of crystal water. Fig. 18b indicate that the the hybrid shows 4 highly intense diffraction peaks with regularly reduced intensities in the low 2θ angle range of 1.5 – 20°, indicating that the as-obtained product is of a highly ordered layered structure. The peaks at $2\theta = 3.836^\circ$, 7.671° , 11.507° , and 15.342° can be indexed to the reflections from (010), (020), (030) and (040) diffraction planes, respectively, when considering the layered structure of MoO_3 along the *b*-axis direction. The interlayer distance (*d*) can be calculated to be $d = 2.306(1)$ nm using a program UnitCell, refined in a cubic

system ($\lambda = 1.54055 \text{ \AA}$) by minimizing the sum of squares of residuals in 2θ . In the 2θ -angle range of $20^\circ - 40^\circ$, there are numerous diffraction peaks with low intensities, as shown in the inset of Fig. 18b. These diffraction peaks are similar to those of molybdic acid (Fig. 18a), and can mainly be attributed to the reflections from the inorganic MoO_6 frames.

Fig. 18(c) shows the XRD pattern of the product obtained by calcining the molybdate-based inorganic-organic hybrid disks at 550°C for 1 h in air. All the diffraction peaks can be readily indexed to an orthorhombic MoO_3 phase ($\alpha\text{-MoO}_3$, space group: Pbnm (62)) according to JCPDS card No. 05-0508. The calculated cell parameters by refining the XRD pattern are $a = 3.964(2) \text{ \AA}$, $b = 13.862(3) \text{ \AA}$ and $c = 3.6991(8) \text{ \AA}$, close to the literature data ($a = 3.962 \text{ \AA}$, $b = 13.858 \text{ \AA}$, $c = 3.697 \text{ \AA}$, JCPDS card No. 05-0508). The $I_{(0k0)}I_{(111)}$ values of the as-obtained $\alpha\text{-MoO}_3$ are obviously larger than those of the literature data, indicating that the as-obtained $\alpha\text{-MoO}_3$ sample is of an obvious preferred orientation growth along the $(0k0)$ planes.

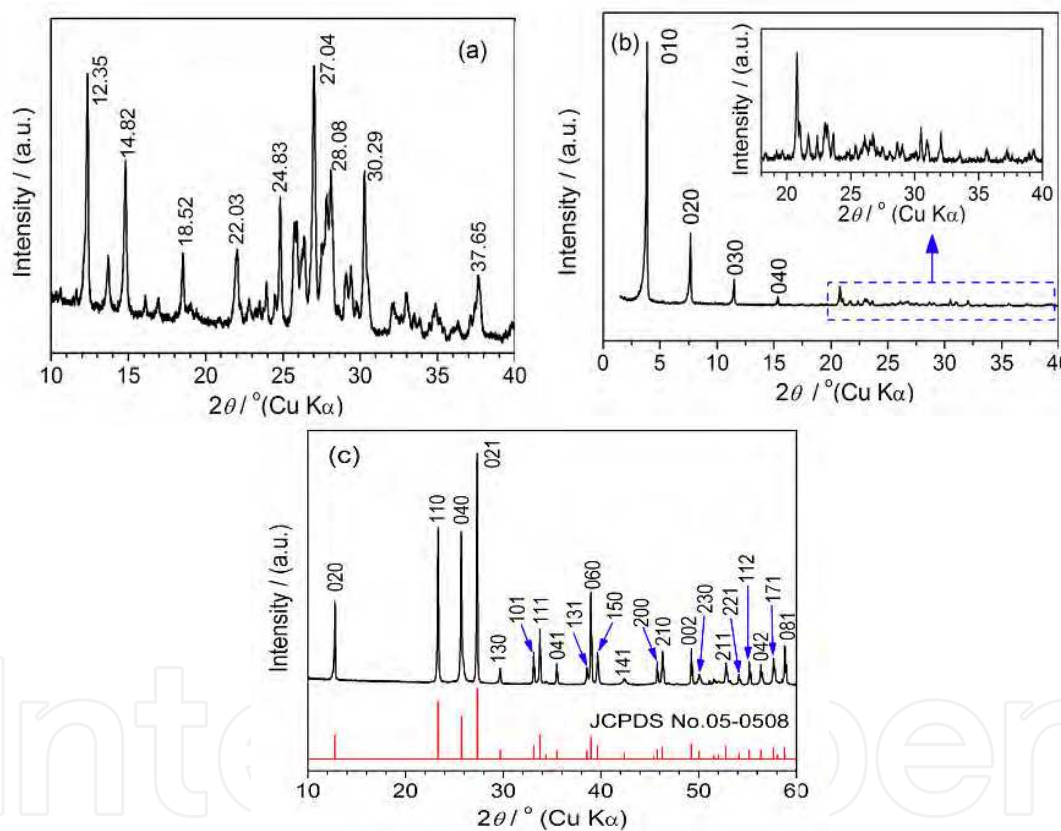


Fig. 18. XRD patterns of (a) commercial molybdic acid; (b) molybdate-based inorganic-organic hybrid compound derived from the reaction of commercial molybdic acid with n -octylamine in ethanol ($n_{\text{Mo}}:n_{\text{N}}=1:5$); (c) MoO_3 nanocrystals derived by calcining the molybdate-based hybrid compound at 550°C (the inset is the data from JCPDS card No. 05-0508). Reprinted with permission from *J. Mater. Chem.*, 2011, 21(25), 9332-9342. Copyright 2011 Royal Society of Chemistry.

Figs. 19a-d show the SEM images of the commercial molybdic acid and the resultant molybdate-based hybrid compound obtained with $n_{\text{Mo}}:n_{\text{N}} = 1:5$. As Figs. 19a-b show, the commercial molybdic acid consists of large aggregates with sizes of $10 - 15 \mu\text{m}$, and the

original grains are platelike particles with side sizes of 1 – 3 μm . Figs. 19c–d show the morphology of the hybrid product, consisting of separate disklike particles, with thicknesses of $1.55 \pm 0.4 \mu\text{m}$ and apparent side sizes of $5.2 \pm 1.7 \mu\text{m}$. The average side-to-thickness ratio of the as-obtained disks is 3.5. Figs. 19e –f show the SEM images of the $\alpha\text{-MoO}_3$ sample derived by calcining the molybdate-based inorganic–organic hybrid disks at 550 °C for 1 h in air. The SEM images with various magnifications suggest that the $\alpha\text{-MoO}_3$ sample is composed of platelike nanocrystals with a good dispersibility in a large view field (Fig. 19e). The platelike particles are of side sizes of 1 – 10 μm and thicknesses of 50 – 150 nm. The platelike morphology of the as-obtained $\alpha\text{-MoO}_3$ sample makes them tend to lie down along a substrate and their large surfaces parallel to the substrate, because of their large side-to-thickness ratios. Considering the preferred growth of the (0k0) planes together with their platelike morphology, one can safely conclude that the as-obtained $\alpha\text{-MoO}_3$ nanoplates have a shortest side along the *b*-axis, that is, the thickness of the $\alpha\text{-MoO}_3$ nanoplates is along the *b*-axis (i.e., the [0k0] direction).

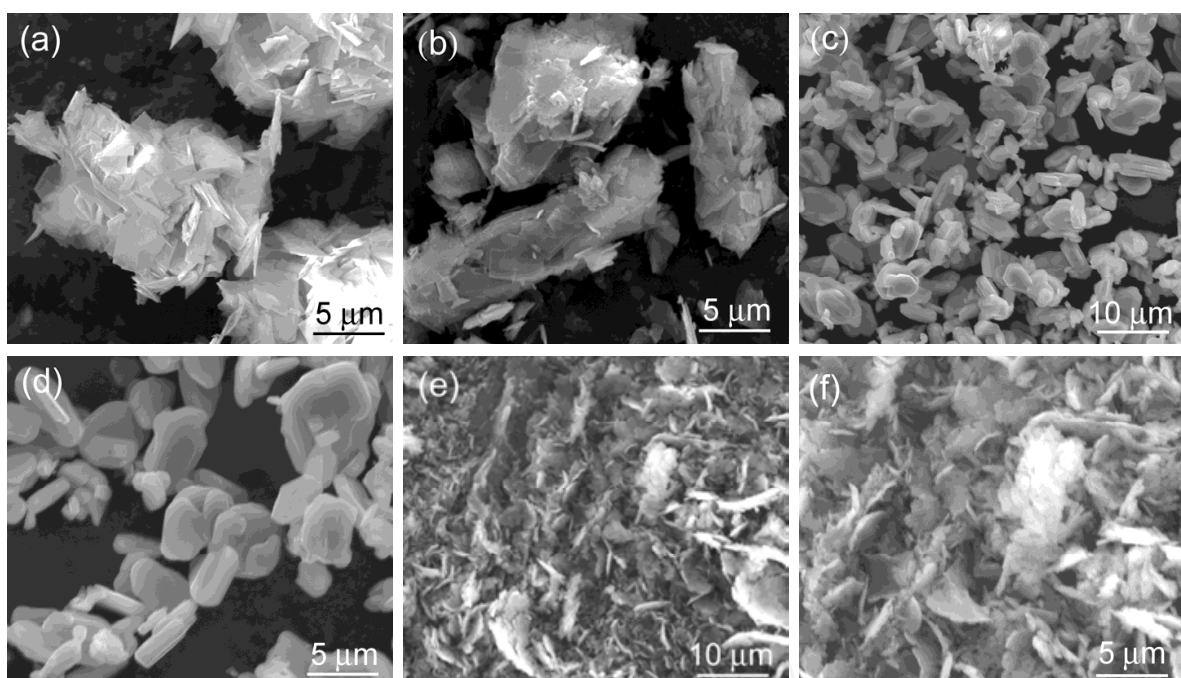


Fig. 19. SEM images of (a, b) commercial molybdic acid; (c, d) molybdate-based hybrid compound derived from the reaction of commercial molybdic acid with *n*-octylamine in ethanol ($n_{\text{Mo}}:n_{\text{N}}=1:5$); and (e,f) $\alpha\text{-MoO}_3$ nanocrystals derived by calcining the molybdate-based hybrid compound at 550 °C for 1 h in air. Reprinted with permission from *J. Mater. Chem.*, 2011, 21(25), 9332-9342. Copyright 2011 Royal Society of Chemistry.

Fig. 20 shows the TG-DTA curves of the inorganic–organic hybrid disks. The TG curve in Fig. 20a shows that there are four obvious mass-loss stages: (I) 20 – 210 °C with a mass loss of 28%, (II) 210 – 340°C with a mass loss of 11%, (III) 340 – 550 °C with a mass loss of 28 %, and (IV) 700 – 900 °C with a mass loss of 27%. Fig. 20b shows the corresponding DTA result. In stage I, there are two weak endothermic peaks at 136 °C and 185 °C, due to desorption of *n*-octylammonium ions/molecules and the decomposition of crystal water in the Mo–O frames, respectively. The corresponding mass loss of 28% attributes to the removal of the

adsorbed *n*-octylammonium ions / molecules and crystal water. In stage II, there are two strong exothermal peaks at around 249 and 280 °C, respectively, attributed to the oxidation of the organic $-(\text{CH}_2)_n-$ chains in the hybrid compound. The corresponding mass loss (11%) is due to release of small volatile molecules resulted from the oxidation of long *n*-alkyl chains. The resultant inorganic carbon species formed in stage II then combust at elevated temperatures of 340 – 550 °C, confirmed by the strong exothermal peak at 460 °C, and the mass loss of 28% in stage III. During the temperature range of 550 – 700 °C, there are no detectable changes either in the TG curve or in the DTA curve, indicating that a thermally stable α -MoO₃ phase is formed. When the temperature is higher than 700 °C, *i.e.*, stage IV, there is a weak endothermic peak at around 786 °C, accompanying with a mass loss of 33%. The melting and evaporating behaviors of α -MoO₃ account for the endothermic peak and the large mass loss in stage IV. If the composition of the molybdate-based inorganic-organic hybrid compound can be expressed as $(\text{C}_8\text{H}_{17}\text{NH}_3)_x\text{H}_{2-x}\text{MoO}_4$, and the product calcined at a temperature higher than 550°C is MoO₃, the *x* value can be calculated to be about 2.12 according to the total mass loss of 67% at 20 – 520 °C. Therefore, the composition of the molybdate-based inorganic-organic hybrid compound can be described as $(\text{C}_8\text{H}_{17}\text{NH}_3)_2\text{MoO}_4$.

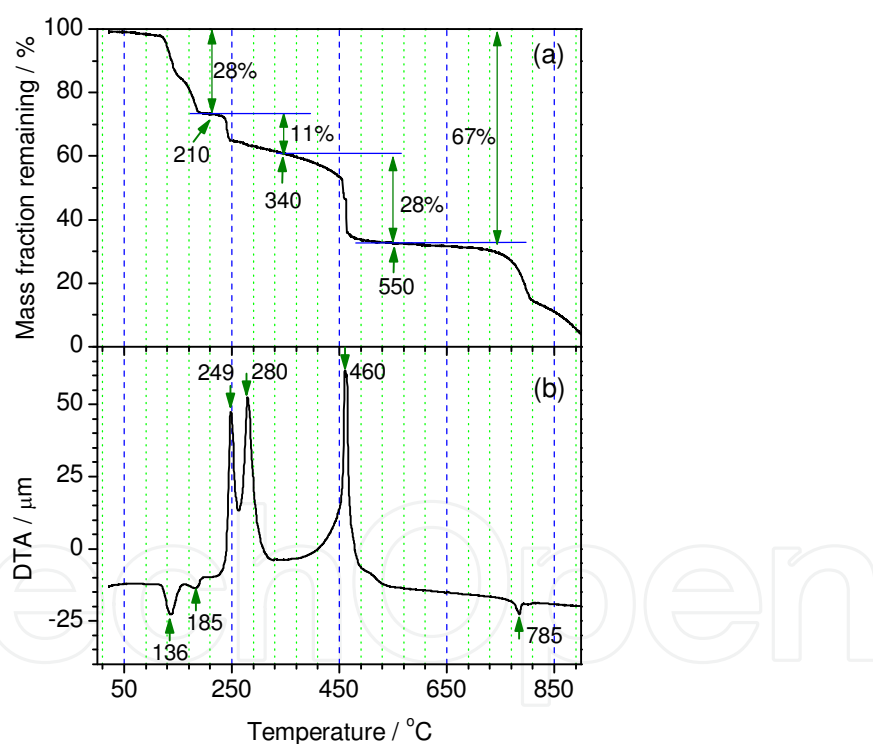


Fig. 20. (a) TG and (b) DTA curves of the molybdate-based hybrid compound obtained from the reaction of commercial molybdic acid with *n*-octylamine in ethanol ($n_{\text{Mo}}:n_{\text{N}}=1:5$). Reprinted with permission from *J. Mater. Chem.*, 2011, 21(25), 9332-9342. Copyright 2011 Royal Society of Chemistry.

Fig. 21 shows the typical TEM observations of the α -MoO₃ nanoplates obtained by calcining the molybdate-based inorganic-organic hybrid disks at 550 °C for 1 h in air. Most of the α -MoO₃ nanoplates take on a quadrilateral platelike shape with a lateral length of 1 – 2 μm

(Fig. 21a), and some α -MoO₃ nanoplates are partially overlapped with each other. Fig. 21b shows a typical individual α -MoO₃ nanoplate with a dimension of 1000 nm \times 600 nm and its thickness is very thin (several nanometers) judged by the shallow contrast grade. The typical SAED pattern (Fig. 21c) of the individual α -MoO₃ nanoplate can be indexed to an orthorhombic α -MoO₃ phase with a zone axis along the [010] direction, and indicates that the α -MoO₃ nanoplate is of a single-crystal structure and has a thin and uniform thickness. The HRTEM image (Fig. 21d) of an edge of the α -MoO₃ nanoplate indicates that the α -MoO₃ nanoplate is single-crystal. The distances of lattice stripes are about 0.40 nm and 0.37 nm, corresponding to the (100) and (001) planes of the α -MoO₃ phase, respectively. The as-obtained α -MoO₃ nanoplates may consist of thinner sub-plates because of the formation process on the basis of interaction chemistry. Fig. 21e shows a typical example. The α -MoO₃ nanoplate is composed of three super-thin subplates, which overlap loosely with each other. Fig. 21f shows an HRTEM image of a tip of one of the subplates, and the clear lattice stripes indicates the sub-plate is also of a well-defined single-crystal structure.

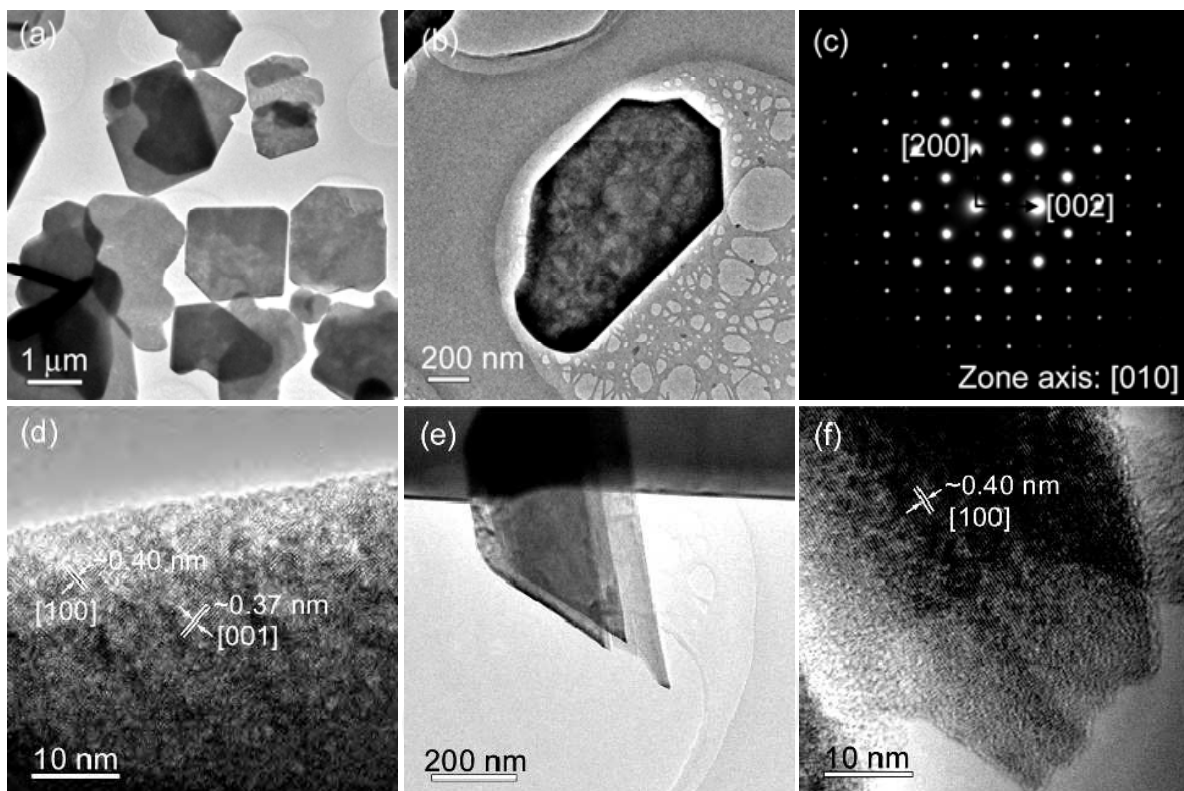


Fig. 21. (a) A low-magnification TEM image of α -MoO₃ nanoplates; (b) a TEM image, (c) an SAED pattern and (d) an HRTEM image of an individual α -MoO₃ nanoplate; (e) a TEM image of laminated α -MoO₃ nanoplates, and (f) an HRTEM image of the tip of an α -MoO₃ nanoplate. Reprinted with permission from *J. Mater. Chem.*, 2011, 21(25), 9332-9342. Copyright 2011 Royal Society of Chemistry.

Fig. 22 shows a typical Raman spectrum of the α -MoO₃ nanoplates. The vibration modes appearing in the frequency ranges of 1000 – 600 cm⁻¹ and 600 – 200 cm⁻¹ correspond to the stretching and deformation modes, respectively. The narrow band at 994 cm⁻¹ is assignable to the antisymmetric ν (Mo=O₁) stretching (A_g), in which the bonding aligns along the *b* axis

direction. The strong band at 819 cm^{-1} represents the symmetric $\nu(\text{Mo}-\text{O}_3-\text{Mo})$ stretching (A_g) with the bonding aligning along the a -axis direction. The weak and broad bands at 666 and 470 cm^{-1} are ascribable to the antisymmetric $\nu(\text{Mo}-\text{O}_2-\text{Mo})$ stretching (B_{2g}) and bending (A_g), respectively. The bands at 377 and 364 cm^{-1} correspond to the $\delta(\text{O}_2=\text{Mo}=\text{O}_2)$ scissor (B_{1g} and A_g modes). The band at 336 cm^{-1} is characteristic of the $\delta(\text{O}_3-\text{Mo}-\text{O}_3)$ deformation (B_{1g}). The band at 282 cm^{-1} and a weak shoulder centered at 289 cm^{-1} correspond to the $\delta(\text{O}_1=\text{Mo}=\text{O}_1)$ wagging (B_{2g} and B_{3g} , respectively). The bands at 242 and 215 cm^{-1} correspond to the $\delta(\text{O}_2-\text{Mo}-\text{O}_2)$ scissor (B_{3g} and A_g modes, respectively).

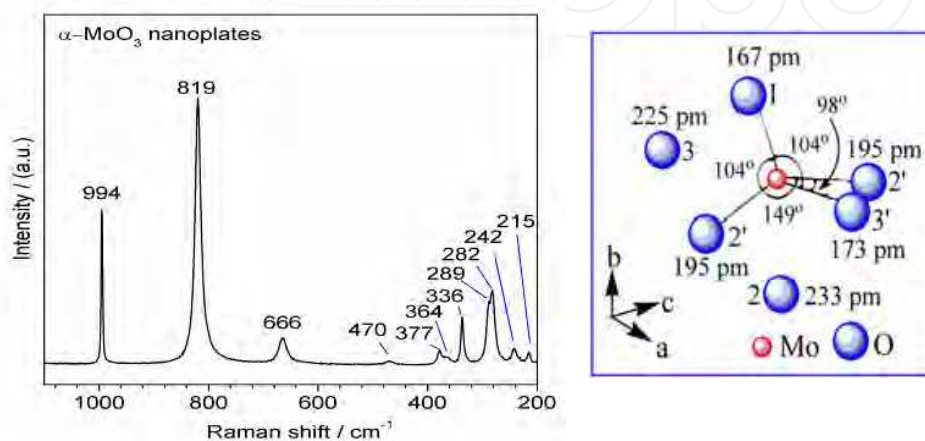


Fig. 22. A Raman spectrum of $\alpha\text{-MoO}_3$ nanoplates derived from molybdate-based inorganic-organic hybrid disks. Reprinted with permission from *J. Mater. Chem.*, 2011, 21(25), 9332-9342. Copyright 2011 Royal Society of Chemistry.

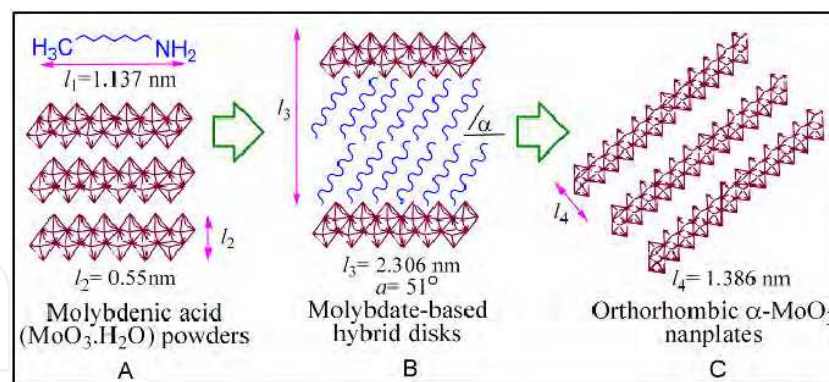


Fig. 23. A schematic of the formation mechanism for molybdate-based inorganic-organic hybrid compound and the resultant $\alpha\text{-MoO}_3$ nanoplates. Reprinted with permission from *J. Mater. Chem.*, 2011, 21(25), 9332-9342. Copyright 2011 Royal Society of Chemistry.

Fig. 23 shows the schematic of the formation mechanisms for the molybdate-based inorganic-organic hybrid disks and the $\alpha\text{-MoO}_3$ nanoplates. In the stage of A \rightarrow B, molybdic acid reacts with *n*-octylamine via an acid-base mechanism, where an intercalation and reorganization process is undergone. The length of an *n*-octylamine molecule can be evaluated to be $l_1=1.137\text{ nm}$, according to the length (0.248 nm) of a CH_3NH_2 molecule and the length (0.127 nm) per $-\text{CH}_2-$. The contribution ($l_0 = 1.756\text{ nm}$) of the organic species to

the interlayer distance can be calculated by subtracting the thickness ($l_2 = 0.55$ nm) of the double MoO_6 layer from the interlayer distance ($l_3 = 2.306$ nm). The thickness (l_0) of the organic species is larger than the length (l_1) of an *n*-octylamine molecule (or an *n*-octylammonium ion), and the *n*-octyl chains, therefore, take a double-layer arrangement with a tilt angle of $\alpha = \sin^{-1}(l_0/2l_1) = 51^\circ$ (Fig. 23B), which is in good agreement with the previously reported result (50.8°). The organic layers of molybdate-based inorganic–organic hybrid disks are removed by a thermal treating process at $550\text{ }^\circ\text{C}$ and the platelike $\alpha\text{-MoO}_3$ nanocrystals are obtained, as shown as the stage of B→C. The synthesis of $\alpha\text{-MoO}_3$ nanoplates can be seen as a pseudo-topochemical transformation, where the platelike morphology is from the precursors to the final products. The possible chemical reactions can be described as Eqs. 1-2.

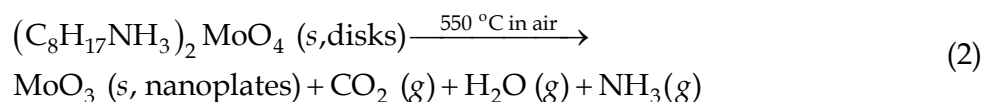
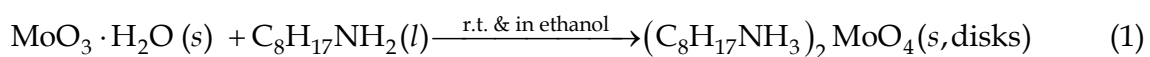


Fig. 24 shows a typical SEM image of the as-obtained $\alpha\text{-MoO}_3$ product obtained by calcining commercially available $\text{MoO}_3\text{-H}_2\text{O}$ powders at $550\text{ }^\circ\text{C}$ for 1 h in air. The particulate shapes are the dominant morphology for the $\alpha\text{-MoO}_3$ sample obtained directly from $\text{MoO}_3\text{-H}_2\text{O}$ powders, and most of the $\alpha\text{-MoO}_3$ particles are conglutinated to form large agglomerates. This comparative investigation indicates that molybdate-based inorganic–organic hybrid disks are necessary in the formation of singel-crystal $\alpha\text{-MoO}_3$ nanoplates with a large diameter-to-thickness ratio.

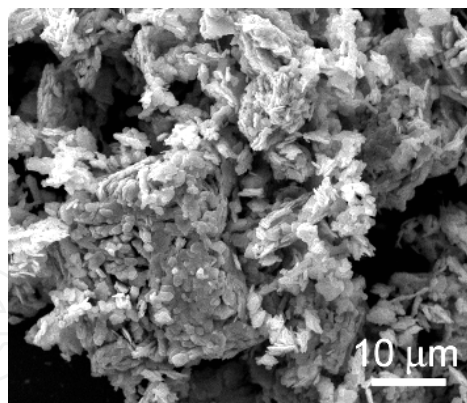


Fig. 24. An SEM image of particulate MoO_3 nanocrystals derived by calcining commercial molybdic acid ($\text{MoO}_3\text{-H}_2\text{O}$) at $550\text{ }^\circ\text{C}$ for 1 h in air. Reprinted with permission from *J. Mater. Chem.*, 2011, 21(25), 9332-9342. Copyright 2011 Royal Society of Chemistry.

5. Topochemical conversion of tungstate-based inorganic–organic hybrid belts to $\beta\text{-W}_2\text{N}$ nanoplates^[8]

5.1 Material synthesis and characterization

Typically, 0.5 g of tungstate-based inorganic–organic hybrid nanobelts was placed in a semi-cylindrical Al_2O_3 crucible, and the crucible was then inserted to the center of a tubular

quartz furnace ($\phi 500 \text{ mm} \times 1000 \text{ mm}$) in a lying manner. The gas-out end of the quartz tube was loosely stuffed with a porous cylindrical alumina tile. The quartz tube was first purged with a high-pure Ar gas (100 mL/min) for 1 h. After the Ar gas was closed and the NH₃ gas was simultaneously opened with a flux of 80 mL/min, the furnace was rapidly heated to 500 °C with a heating rate of 25 °C /min, and then slowly heated from 500 °C to 650–800 °C with a heating rate of 2 °C /min. After kept at 650–800 °C for 2 h, the furnace naturally cooled down to room temperature under a NH₃-gas condition.

X-ray diffraction (XRD), SEM, TEM, TG-DTA and FT-IR were used to characterize the as-obtained products.

5.2 Results and discussion

A typical XRD pattern of the sample obtained by treating tungstate-based inorganic–organic hybrid nanobelts at 750 °C for 2 h in a NH₃ flow is shown in Fig. 25a. There are four obvious diffraction peaks at 36.4°, 45.1°, 64.0° and 76.2°, which can readily be indexed to the reflections from (111), (200), (220) and (311) planes of the cubic β -W₂N phase, respectively, according to the literature data (JCPDS card No. 25-1257; space group: Pm3m [221], $a = 0.4126 \text{ nm}$). The calculated cell parameters according to the XRD data and the minimum square method are $a = b = c = 0.4133(8) \text{ nm}$, close to the literature data ($a = 0.4126 \text{ nm}$). As Fig. 25a shows, the diffraction peaks are obviously broadened, indicating that the product consists of nanocrystals with very small crystal sizes. According to the Debye-Scherrer equation ($d=0.89\lambda/B\cos\theta$), $\lambda=0.15406 \text{ nm}$, $B\cos\theta = 0.0428$ for the (111) reflection, and the calculated average size of the crystalline β -W₂N grains is about 3.2 nm.

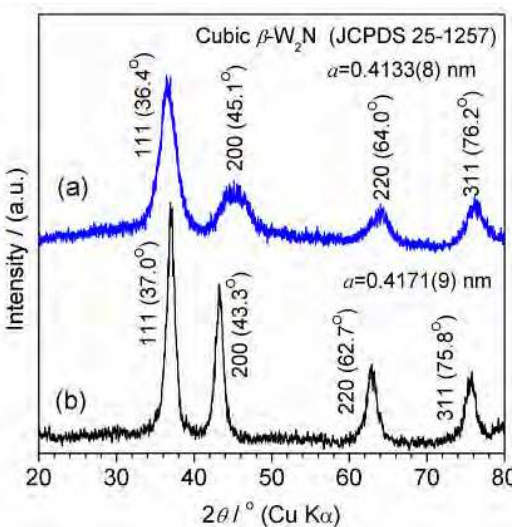


Fig. 25. Typical XRD patterns of (a) cubic β -W₂N nanoplates derived from the tungstate-based inorganic–organic hybrid nanobelts, and (b) cubic β -W₂N nanocrystals derived from commercial H₂WO₄ powders. Reprinted with permission from *J. Solid State Chem.*, 2011, 184(2), 455-462. Copyright 2011 Elsevier.

Fig. 26 shows the typical TEM observations of the β -W₂N nanocrystals derived from tungstate-based inorganic–organic hybrid nanobelts. Fig. 26a shows a low-magnification TEM image, indicating the β -W₂N product consists of well-dispersed nanoplates. Most of the nanoplates are of sharp profiles, including triangles, trapezoids and rectangles. The

enlarged TEM image shown in Fig. 26b corroborates that the β -W₂N nanoplates obtained are not nanorods, but thin nanoplates, according to the shallow contrasts. The contrast from different parts of a nanoplate suggests that some β -W₂N nanoplates are curly or partly scrolled. Fig. 26c shows an individual partly-scrolled β -W₂N nanoplate with an apparent dimension of about 200 nm \times 500 nm. The enlarged TEM image in Fig. 26d shows a β -W₂N nanoplate with a dimension of about 130 nm \times 300 nm. Its contrast indicates the nanoplate is composed of nanoparticles with sizes of several nanometers. The corresponding SAED pattern of the β -W₂N nanoplate (Fig. 26e) is shown in Fig. 26e. The SAED pattern consists of a series of concentric diffraction rings superimposed a series of separate diffraction spots, indicating that the β -W₂N nanoplate is composed of small crystalline nanoparticles. The concentric diffraction rings can be readily indexed to the reflections from the cubic β -W₂N phase. The TEM observations are consistent to the XRD results. The grain sizes (about 3.2 nm) of the β -W₂N product calculated from the XRD result are much smaller than the sizes of the plate-like particles from the TEM observations, suggesting that an individual β -W₂N plate-like particle is not a single crystal, but is composed of a great number of small β -W₂N nanocrystals. This point is corroborated by the corresponding SAED pattern with a series of concentric diffraction rings.

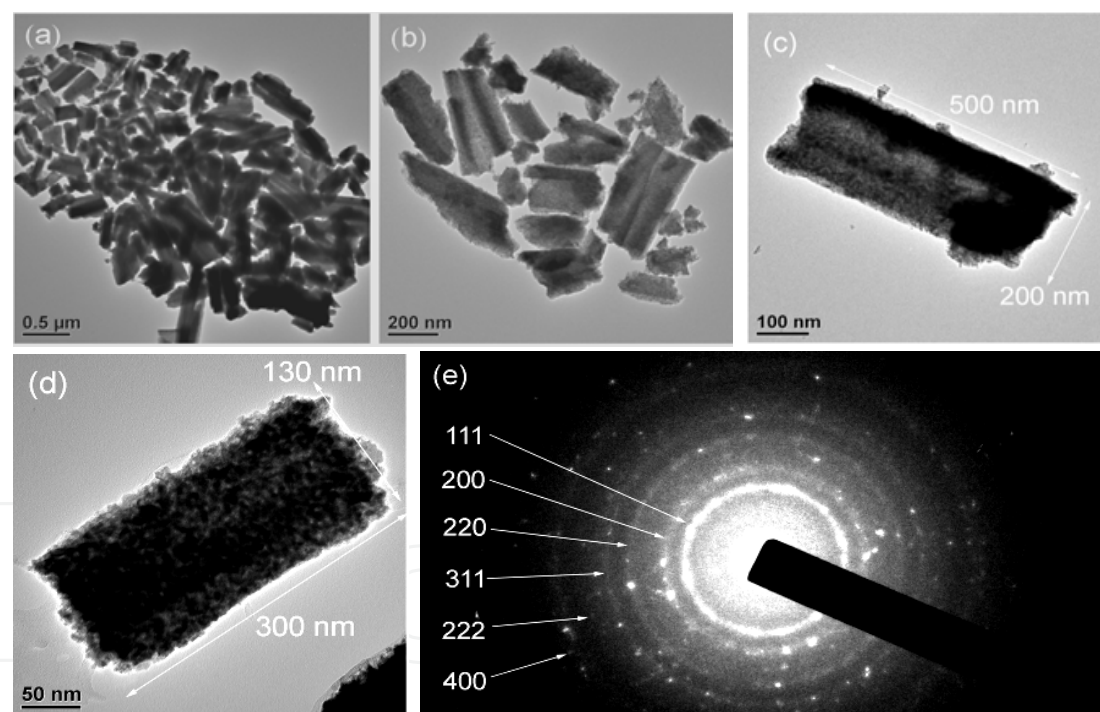


Fig. 26. (a-d) TEM images and (e) SAED pattern of the β -W₂N nanoplates derived from the tungstate-based inorganic–organic hybrid nanobelts. Reprinted with permission from *J. Solid State Chem.*, 2011, 184(2), 455-462. Copyright 2011 Elsevier.

For comparison, tungsten nitride was also synthesized by directly nitridizing commercially available H₂WO₄ powders. Fig. 25b shows the XRD pattern of the as-obtained product by nitridizing H₂WO₄ powders in an NH₃ flow. It can be indexed to be cubic β -W₂N with a calculated cell parameter of $a=0.4171(9)$ nm, a little larger than that [$a=0.4133(8)$ nm] of β -W₂N nanoplates. Fig. 27 shows a typical SEM image of the β -W₂N sample, consisting of

shape-irregular particles, with a large size-distribution (1-5 μm), similar to their precursor of commercial H_2WO_4 powders. The comparative experimental results corroborate that the plate-like morphology of $\beta\text{-W}_2\text{N}$ nanoplates is inherited from the tungstate-based inorganic-organic hybrid nanobelts.

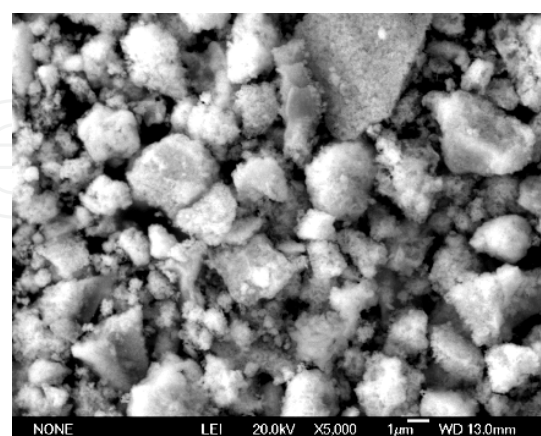


Fig. 27. A typical SEM image of cubic $\beta\text{-W}_2\text{N}$ sample derived from commercial H_2WO_4 powders. Reprinted with permission from *J. Solid State Chem.*, 2011, 184(2), 455-462. Copyright 2011 Elsevier.

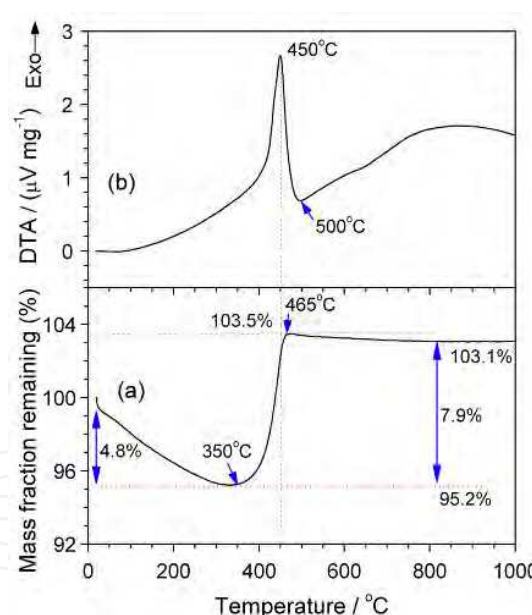


Fig. 28. TG-DTA curves of the $\beta\text{-W}_2\text{N}$ nanoplates derived from the tungstate-based inorganic-organic hybrid nanobelts. Reprinted with permission from *J. Solid State Chem.*, 2011, 184(2), 455-462. Copyright 2011 Elsevier.

Fig. 28 shows typical TG-DTA curves of the $\beta\text{-W}_2\text{N}$ nanoplates derived from tungstate-based inorganic-organic hybrid nanobelts. The TG curve (Fig. 28a) shows that there is a mass loss of 4.8% from room temperature to 350 °C, followed by a sharp mass gain of 8.3% from 350 °C to 465 °C. There is a small mass loss of 0.4% at 465–800 °C. Fig. 28b shows the corresponding DTA curve, with a sharp exothermal peak between 400 – 500 °C, and weak

and broadened exothermal peaks in the temperature regions of 100 – 400 °C and 500 – 800 °C. Considering the TG result together with its corresponding DTA curve, the large mass loss with a sharp exothermal peak at 350 – 465 °C is mainly due to the oxidation of β -W₂N to WO₃, and the slow mass losses and their corresponding weak exothermal peaks at 100 – 400 °C and 500 – 800 °C should be due to the oxidation of the residual C species. Supposing that β -W₂N and residual C are completely oxidized to be WO₃ and CO₂, respectively, the content of the β -W₂N phase in the sample can be calculated to be 91.7% according to the total mass gain of 3.1% between 100 °C and 800 °C. It is noted that the oxidation temperature region of the as-obtained β -W₂N nanoplates is 350–500 °C.

6. Topochemical conversion of tungstate-based inorganic–organic discs to hierarchical tungsten carbide micro-/nanocrystals^[9]

6.1 Material synthesis and characterization

The tungstate-based inorganic–organic hybrids were synthesized by a reaction between H₂WO₄ and *n*-octylamine in heptane. Typically, 10 g of H₂WO₄ powders was moistened by 5 mL of distilled water, and the H₂O-moistened H₂WO₄ was then dispersed in the mixture of 0.4 mol of *n*-octylamine and 530 mL of heptane under a constant magnetic stirring at room temperature. The molar ratio of H₂WO₄ to *n*-octylamine was about 1:10 and the volume ratio of *n*-octylamine to heptane was 1:8. After a reaction time of more than 48 h, the resulting white solid was collected by centrifugation, washed with ethanol, and then dried under a reduced pressure at room temperature for 30 h. The dried product, a tungstate-based inorganic–organic hybrid compound, was used as the precursor for the synthesis of tungsten carbide micro-/nanocrystals.

Typically, 0.3 g of the hybrid precursor was placed in the bottom of the quartz tube with a diameter of 10 mm and a length of 25 cm. The quartz tube was then vacuumized to 2×10^{-3} Pa and sealed. The sealed quartz tube was placed in an electrical resistance furnace, and thermally treated at 750~1050 °C with a heating rate of 5 °C/min for 2~10 h. After a given reaction time, the sealed tube was cooled naturally to room temperature. The black powders at the bottom of the quartz tube were carefully collected.

X-ray diffraction (XRD), SEM and FT-IR were used to characterize the as-obtained intermediate and final products.

6.2 Results and discussion

Fig. 29 shows the XRD patterns of the products obtained by thermally treating the tungstate-based inorganic–organic hybrid compound at 750~1050 °C for 2~10 h in a sealed quartz tube. The product obtained at 750 °C for 5 h, Fig. 29a, can be readily indexed to monoclinic WO₂ (JCPDS card No. 32-1393), and no other phases are observed. The product obtained at 800 °C for 5 h, Fig. 29b, has a major phase of monoclinic WO₂ and minor phases of cubic β -W_{40.9}N_{9.1} (JCPDS No. 03-1031) and hexagonal WC (JCPDS No. 25-1047). When the thermal treating temperature increases to 850 °C, the phases of WO₂ and β -W_{40.9}N_{9.1} disappear, but a new phase of hexagonal α -W₂C (JCPDS No. 35-0776) occurs, as shown in Fig. 29c. With increases in thermal treating time from 5 h to 10 h, the hexagonal WC becomes the dominant phase, and a very small amount of α -W₂C and cubic W (JCPDS No. 04-0806) coexist, as shown as Figs. 29c-d. The product obtained at 950 °C for 5h mainly consists of hexagonal WC, coexisting with a very small amount of α -W₂C (Fig. 29e). An elevated treating temperature

and shortened treating time, e.g., at 1000 °C for 2 h, can also achieve a product with major compositions of hexagonal WC and α -W₂C, as shown in Fig. 29f. The product obtained at 1050 °C for 2 h (Fig. 29g) is composed of a pure hexagonal WC phase.

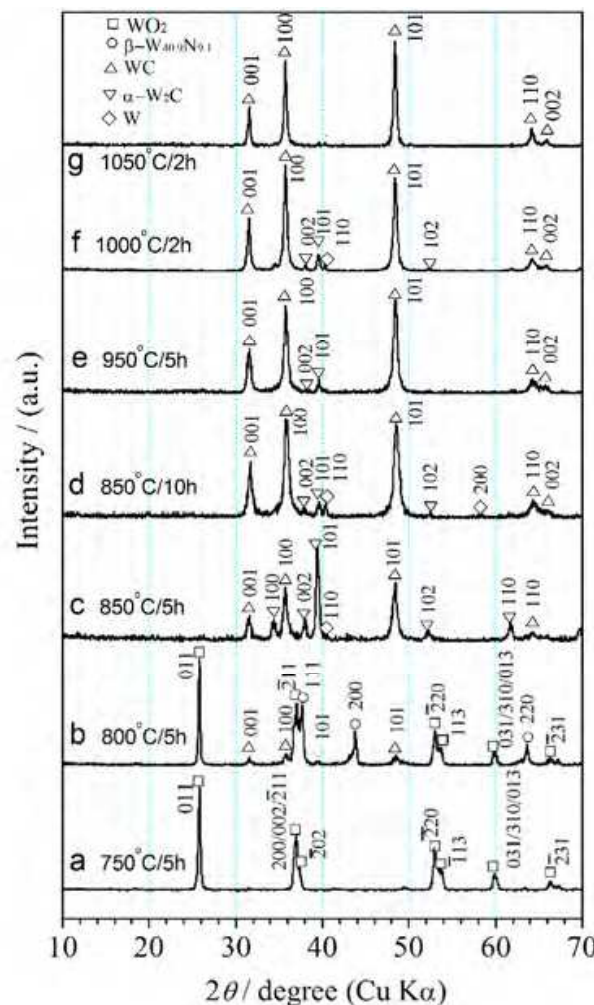


Fig. 29. XRD patterns of the products obtained by thermally treating the tungstate-based inorganic-organic hybrid compound in the sealed quartz tube under various conditions: (a) 750 °C for 5 h, (b) 800 °C for 5 h, (c) 850 °C for 5 h, (d) 850 °C for 10 h, (e) 950 °C for 5 h, (f) 1000 °C for 2 h and (g) 1050 °C for 2 h. (Δ) WC (JCPDS No.25-1047), (∇) α -W₂C (JCPDS No.35-0776), (\diamond) W (JCPDS No.04-0806), (\circ) β -W_{40.9}N_{9.1} (JCPDS No.03-1031) and (\square) WO₂ (JCPDS No.32-1393). Reproduced with permission from *J. Am. Ceram. Soc.*, 2010, 93(12), 3997-4000. Copyright 2010 John Wiley and Sons.

Fig. 30 shows the typical SEM images of the C₈N@H₂WO₄ hybrid (Fig. 30a) and the corresponding WC product obtained at 1050 °C for 2 h with various magnifications (Figs. 30b-d). The hybrid compound takes on a plate-like morphology, with side-sizes of about 1 μ m, as shown in Fig. 30a. According to the FT-IR spectrum (the inset of Fig. 30a), the tungstate-based inorganic-organic hybrid compound consists of inorganic W-O layers and organic ammonium ions. The TG-DTA curves suggested the mass remaining is 65 % after thermal treating at 600 °C in an air flow. A low-magnification SEM image in Fig. 30b indicates the WC product consists of spherical microparticles, which are well dispersed in a

large view field. Fig. 30c shows an enlarged SEM image, indicating that the spherical microparticles are porous aggregates with an apparent size range of 5~15 μm . A high-magnification SEM image, as shown in Fig. 30d, indicates that the porous microparticles are loose aggregates of WC nanoparticles with a particle size of 100~250 nm. The result of laser particle size analysis indicated that the apparent particle sizes of the WC powders obtained at 1050 °C for 2 h range in 4.0~18.0 μm , with a peak size of 8.6 μm . The above result is consistent with the SEM observations (Figs. 30b & c). The specific surface area of the WC powders obtained at 1050 °C for 2 h is 1.7 m^2/g . Their average diameter estimated according to the specific surface area is about 200 nm, which is very close to the high-resolution SEM observation (Fig. 30d). The molar ratio of W to C of the WC sample obtained at 1050 °C for 2 h is close to 1:1 according to the EDS spectra.

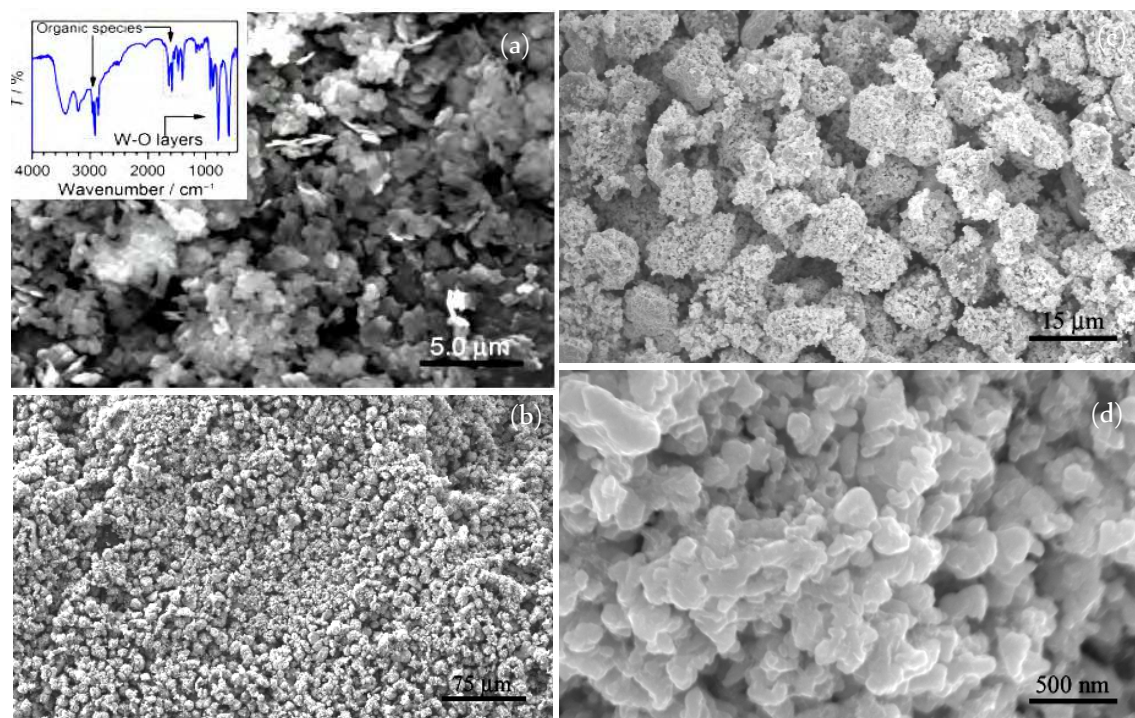
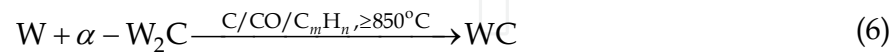


Fig. 30. (a) A typical SEM image of the as-obtained $\text{C}_8\text{N}@H_2\text{WO}_4$ hybrid derived from a reaction between $H_2\text{O}$ -moisted $H_2\text{WO}_4$ powders and *n*-octylamine (the inset is its FT-IR spectrum); (b-d) SEM images with various magnifications of the WC powders obtained by treating the $\text{C}_8\text{N}@H_2\text{WO}_4$ hybrid at 1050 °C for 2h. Reproduced with permission from *J. Am. Ceram. Soc.*, 2010, 93(12), 3997-4000. Copyright 2010 John Wiley and Sons.

The formation process of hexagonal WC particles undergoes the following steps according to the XRD results. (1) The pyrolysis of the tungstate-based inorganic-organic hybrid precursor leads to formation tungsten oxides (e.g., WO_2) and some species containing carbon and nitrogen in the sealed quartz tube. (2) The species containing carbon and nitrogen react with the tungsten oxides, and form $\beta\text{-W}_{40.9}\text{N}_{9.1}$, $\alpha\text{-W}_2\text{C}$, W and WC. (3) The phases of $\beta\text{-W}_{40.9}\text{N}_{9.1}$, $\alpha\text{-W}_2\text{C}$ and W further react with the C-containing species, and finally form a hexagonal WC phase by elevating the reaction temperature and prolonging the reaction time.

In the sealed quartz tube, the pyrolyzed organic ammonium ions emit excess C-containing species relative to the amount of W, and this is helpful for the formation of a pure WC

phase. The excess C forms carbon films and carbon beads in the other end wall of the quartz tube. The above results are validated by EDS examination on the samples collected from different parts of the quartz tube. The possible chemical reactions can be described as Eqs.3–6.



7. Typical applications of WO_3 and MoO_3 nanoplates

7.1 Photocatalysts for water splitting [6]

Fig. 31 shows the UV/Vis spectra of the as-obtained WO_3 nanoplates and commercially available WO_3 powders. The on-set value of the absorption band of the synthesized WO_3 nanoplates was *ca.* 466 nm (spectrum A), by which the energy band gap was estimated as *ca.* 2.67 eV. Although the energy gap of the WO_3 nanoplates is a little larger than that of the bulk WO_3 (2.58 eV) due to the quantum size effect, the WO_3 nanoplates are still able to absorb a majority of solar energy and can be an efficient photocatalyst for the visible-light utilization.

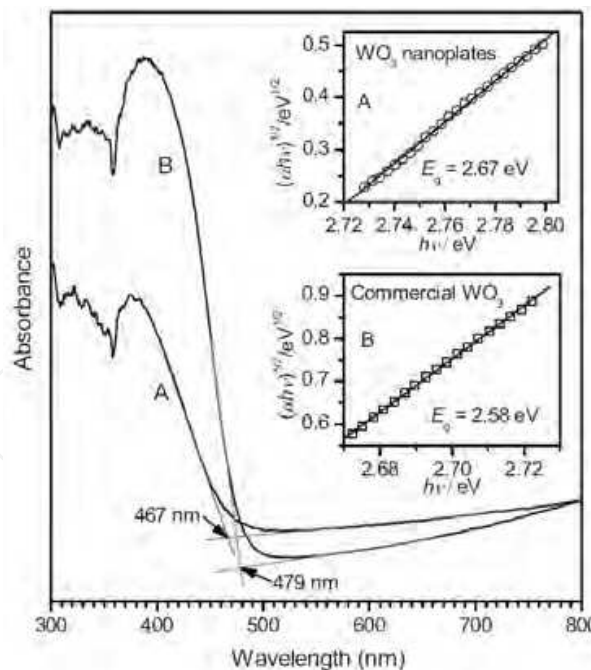


Fig. 31. UV/Vis absorption spectra of A) as-obtained WO_3 nanoplates and B) commercially available WO_3 powders. The insets are the plots of $(ah\nu)^{1/2}$ versus $h\nu$, by which the values of the energy band gaps of the as-obtained WO_3 nanoplates and the commercial WO_3 powders are determined as 2.67 and 2.58 eV, respectively. Reprinted with permission from *Small*, 2008, 4(10), 1813-1822. Copyright 2008 Wiley-VCH Verlag GmbH & Co. KGaA.

Fig. 32 shows the results of the visible-light-induced water splitting for oxygen (O_2) generation using the WO_3 nanoplates as the photocatalyst. For comparison, the commercial WO_3 powders were also used as the photocatalyst for water splitting under the same experimental conditions. As Fig. 32 shows, the amount of O_2 generated using WO_3 nanoplates as the photocatalyst is larger than the case of commercial WO_3 powders by an order of magnitude. The enhanced photocatalytic properties should be attributed to the superhigh specific surface areas and high crystallinity of the synthesized single-crystal WO_3 nanoplates.

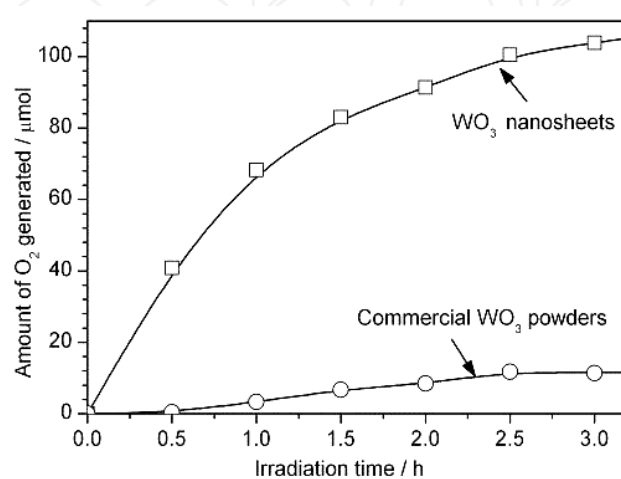


Fig. 32. Plots of the amount of O_2 generated vs. the irradiation time (0.6 g of WO_3 in 300 mL of 0.05 M $AgNO_3$ aqueous solution; visible light irradiation from an 18 W straight-tube fluorescence lamp). Reprinted with permission from *Small*, 2008, 4(10), 1813-1822. Copyright 2008 Wiley-VCH Verlag GmbH & Co. KGaA.

7.2 Sensitive materials for chemical sensors [10,11]

7.2.1 Fabrication of sensors

WO_3 (or α - MoO_3) nanoplates (or nanoparticles) were mixed with a small amount of de-ionized H_2O to form WO_3 (α - MoO_3) pastes in a glass dish. The as-obtained pastes were then brush-coated onto the surfaces of an Al_2O_3 microtube with four Pt electrodes (Fig. 33a). After the WO_3 coating was air-dried, the coating process was repeated until a complete coating was formed. The Al_2O_3 microtubes coated with WO_3 (α - MoO_3) nanoplates were then fixed to a special pedestal with 6 poles (Fig. 33c) by welding the four Pt electrodes to 4 poles of the pedestal, respectively. A heating coil (Fig. 33b) was then inserted through the Al_2O_3 microtube and its two ends were welded to the other two poles of the pedestal. A photograph of the as-obtained WO_3 (α - MoO_3) sensor was shown in Fig. 33d.

7.2.2 Gas-sensing test system

The sensing properties of WO_3 (α - MoO_3) sensors were measured using a commercial computer-controlled HW-30A system under a static testing condition. The sensors, integrated in a large circuit board with 32 inlet-sites, were encased in a transparent glass chamber with a volume of 13.8 L. The testing system was placed in a ventilating cabinet with a large draught capacity. Various vapors of volatile organic liquids were used as the target gases to characterize the sensing performance of the WO_3 (α - MoO_3) sensors. Volatile organic liquids were sampled using syringe-like samplers with ranges of 1–10 μL . The

operating temperatures were r.t–400 °C, controlled by an electric heating system (applied voltages: 4.2–5.0 V). The relative humidity (RH) of the environment was 35–50%.

The concentrations (ppm) were calculated according to the densities of volatile organic liquids and the volume of the chamber using the following equation:

$$V_t = \frac{10^{-9} V_0 \cdot M \cdot C_t}{22.4 \rho \cdot p} \quad (7)$$

Here, V_t is the required volume of the target liquid (μL), V_0 is the volume of the chamber ($V_0=13.8 \text{ L}$), ρ is the density of volatile organic liquids (g cm^{-3}), M is the mole mass (g mol^{-1}) of volatile organic liquids, p is the rate of purity of volatile organic liquids, and C_t is the concentration (ppm) of volatile organic liquids.

An equivalent circuit of the gas-sensing testing system is shown in Fig. 33e. the sensor (R) is connected in series with a load resistor (R_0) with a known resistance (22–1000 KΩ), and a source voltage (U_0) of 5 V is loaded on the circuit. The system measures the voltages (U) loaded on the resistor R_0 , and the resistances (R) of the WO_3 sensors can therefore be calculated according to Eq. 8.

$$R = \frac{U_0 - U}{U} \times R_0 \quad (8)$$

For reducing gases of alcohols and *n*-type semiconducting sensors, the sensitivity (S_r) is defined as Eq. 9, where R_a and R_g are the resistances of the sensor in air ambient and in alcohol ambient, respectively.

$$S_r = R_a / R_g \quad (9)$$

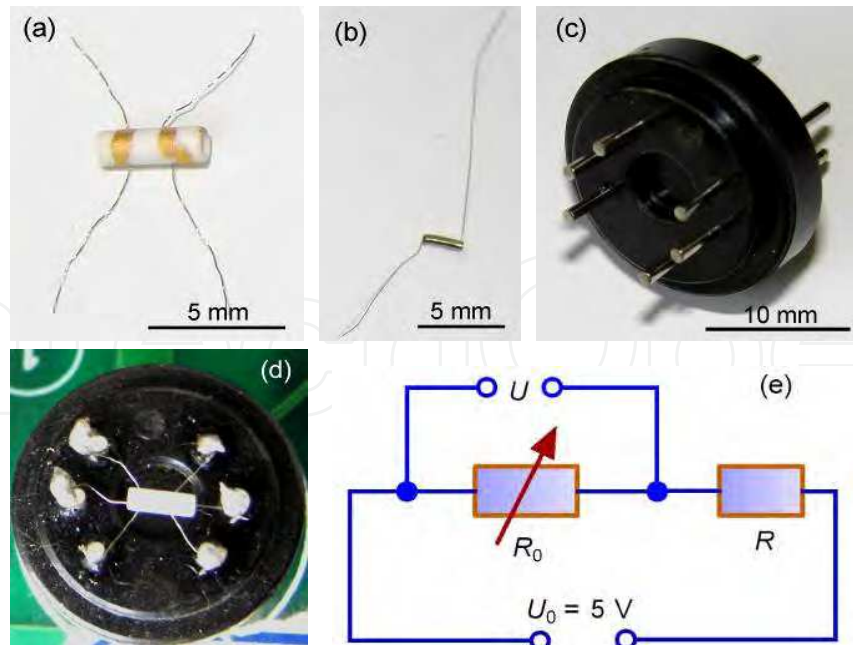


Fig. 33. Components of a sensor and its gas-sensing testing principle: (a) an Al_2O_3 microtube with 4 Pt-electrodes; (b) a heating coil; (c) a pedestal with 6 poles; (d) a photograph of a complete sensor; (e) an equivalent circuit of the alcohol-sensing testing system. Reprinted with permission from *Nanotechnology*, 2010, 21, 035501. Copyright 2010 IOP Publishing Ltd.

The response time (T_{res}) is defined as the time required for the sensor to reach 90% of the stabilized value of its resistance in the presence of the test gas. Similarly, the recovery time (T_{rec}) is defined as the time required for the sensor to reach 10% of the initial steady state value of its resistance after the gas was removed.

7.2.3 Results and discussion

Fig. 34 shows the changing trend of the sensitivities of WO_3 nanoplate sensors as the concentrations of alcohols increase from several ppm to several hundred ppm at an operating temperature of 300 °C. One can find that the sensitivities increase with increases in the concentration of alcohols, including methanol, ethanol, isopropanol and butanol. For methanol, the sensitivity increases from 6 at 10 ppm to 33 at 300 ppm (Fig. 34a). The sensitivity for ethanol increases from 8 at 10 ppm to 38 at 200 ppm (Fig. 34b). For the case of isopropanol, the sensitivity increases from 12 to 75 as its concentration increases from 10 ppm to 200 ppm (Fig. 34c). The sensitivity of WO_3 nanoplate sensors to butanol increases from 31 at 2 ppm to 161 at 100 ppm (Fig. 34d), much higher than the sensitivities to methanol, ethanol or isopropanol. There is a linear relationship between the sensitivity and the concentration for all the tested alcohols. The solid lines in Fig. 34 are the linear fitting results and their linear correlation coefficients (R) are not less than 0.96. When compared the slope coefficients of the fitting equations (inlets in Fig. 34), one can find that the increase rate in the sensitivity to butanol (1.24 per ppm) is much higher than those to isopropanol (0.33 per ppm) and ethanol (0.15 per ppm), whereas the sensitivity to methanol shows a lowest increase rate (0.09 per ppm).

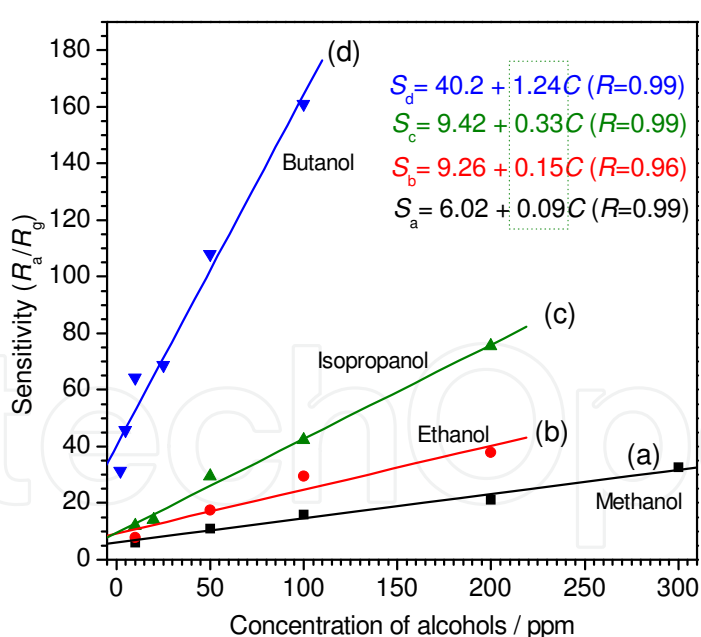


Fig. 34. Sensitivities (R_a/R_g) of the WO_3 nanoplate sensors as a function of alcohol concentration with an operating temperature of 300 °C: (a) methanol, (b) ethanol, (c) isopropanol and (d) butanol. Reprinted with permission from *Nanotechnology*, 2010, 21, 035501. Copyright 2010 IOP Publishing Ltd.

Fig. 35 shows the response and recovery times of the WO_3 nanoplate sensors upon exposure to various alcohol vapors with different concentration levels at an operating temperature of

300 °C. As Fig. 35a shows, the response times of methanol are close to their recovery times at a concentration range of 10–300 ppm, and their values are about 10–14 s. For ethanol, as shown in Fig. 35b, the response times are less than 7 s for the concentration range of 10–200 ppm, but their recovery times are about 10 s, longer than their corresponding response times. The response and recovery times of isopropanol are shown in Fig. 35c. One can find that the response time (less than 10 s) is obviously shorter than its corresponding recovery time (about 15 s). But for the case of butanol, the response time (10–15 s) is longer than its corresponding recovery time (9–10 s), especially in the low concentration range of 2–10 ppm, as shown in Fig. 35d. It is very different from the cases of methanol, ethanol and isopropanol, which have longer recovery times than their corresponding response times. The above-mentioned difference suggests that the semiconductor time response is strongly correlated with the length of alcohol alkyl tails, which have a decreased vapour tension from methanol to butanol.

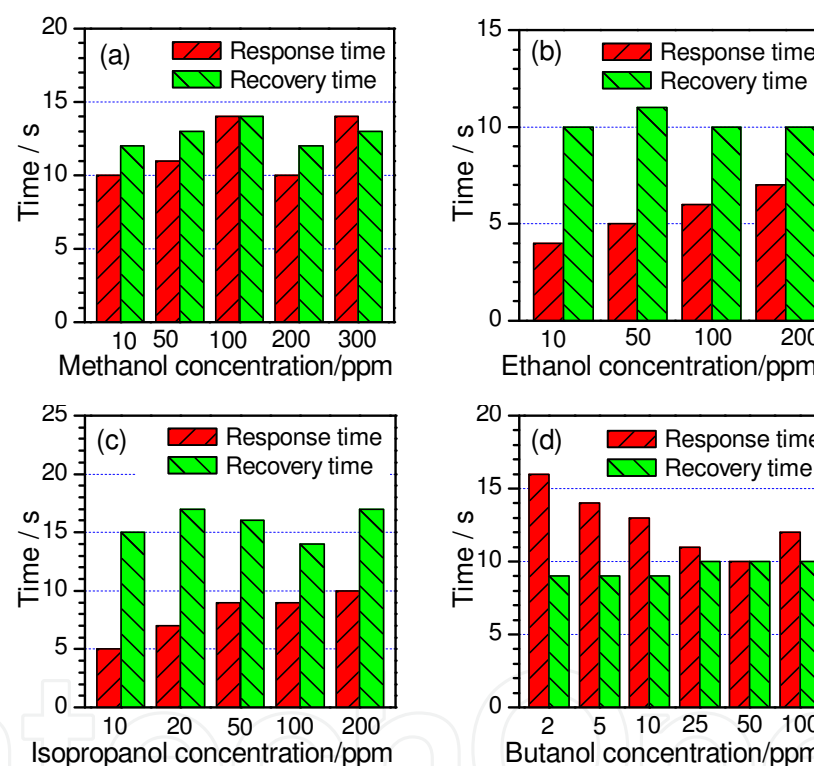


Fig. 35. Response and recovery times of the WO_3 nanoplate sensors operating at 300 °C under various alcohol concentrations: (a) methanol, (b) ethanol, (c) isopropanol and (d) butanol. Reprinted with permission from *Nanotechnology*, 2010, 21, 035501. Copyright 2010 IOP Publishing Ltd.

Fig. 36 shows the acetone-sensing response profiles of the sensors made using the as-obtained WO_3 nanoplates as the sensitive material. Fig. 36a shows a typical response profile of the WO_3 nanoplate sensors operating at 300 °C to acetone vapors with various concentrations from 2 ppm to 1000 ppm. One can find that there are sharp rises and drops in U values when the acetone vapors are injected and discharged, respectively, which indicates that the WO_3 nanoplate sensors are of fast response and recovery speeds to acetone vapors. Fig. 36b shows a similar rapid acetone-sensitive response of the WO_3 nanoplate sensors at an

operating temperature of 250 °C. Fig. 36c shows typical response results of the WO_3 nanoplate sensors operating at 200 °C, and Fig. 36d shows the response curve operating at 100 °C. One can find that when the operating temperature decreases to 100 °C, the change amounts in U obviously decrease, the response speed and the detectable limits decrease, and the response profiles become unstable, as shown in Figs. 36a-d.

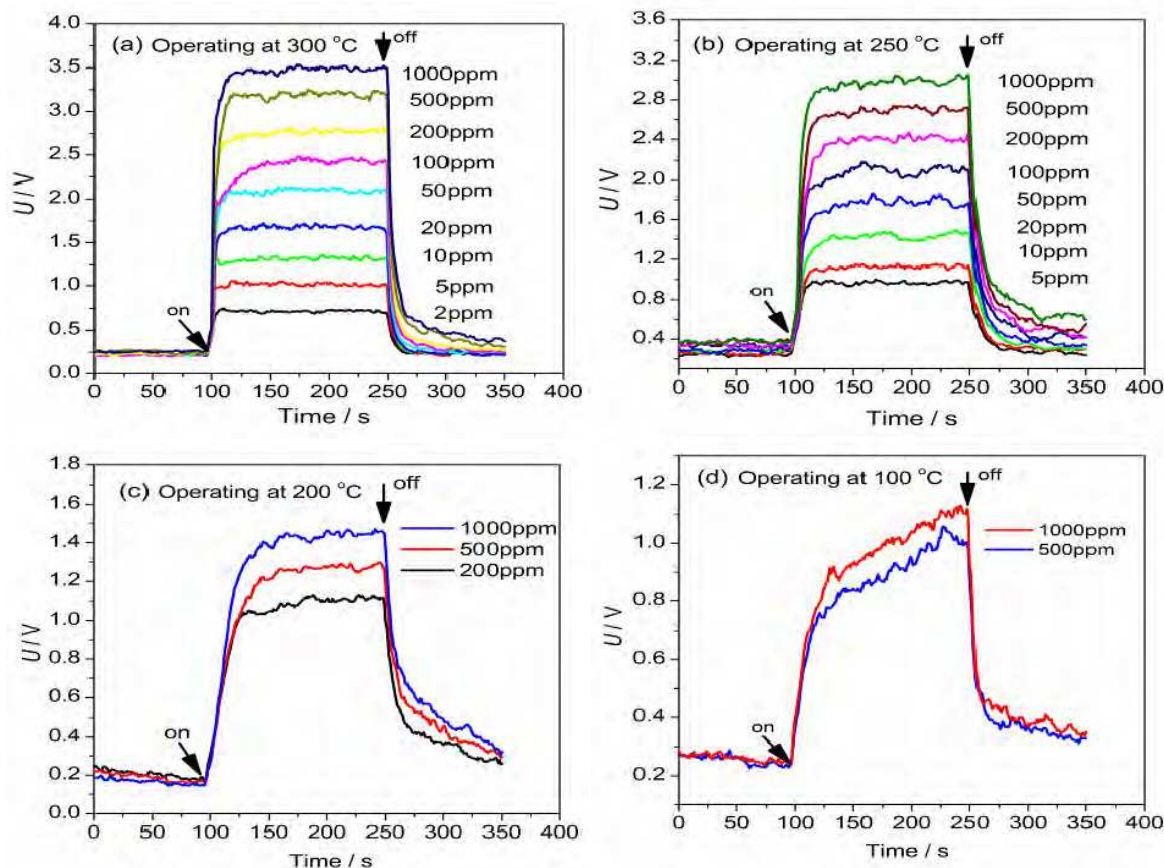


Fig. 36. Acetone-sensing response profiles of the WO_3 nanoplate sensors operating at various temperatures and various acetone vapor concentrations. The R_0 values are 22 k Ω , 100 k Ω , 100 k Ω and 470 k Ω , respectively, for the measurements operating at (a) 300 °C, (b) 250 °C, (c) 200 °C and (d) 100 °C. Reprinted with permission from *Sensor. Actuat. B-Chem.*, 2011, 153(2), 373-381. Copyright 2011 Elsevier.

Fig. 37a presents the sensitivities (R_a/R_g) of the WO_3 nanoplate sensors operating at various temperatures and acetone concentrations. As curve A shows, the sensitivities of the WO_3 nanoplate sensors decrease as the operating temperature decreases in the range of 100–300 °C under the same acetone concentrations in the range of 2–1000 ppm. Also, we can find that the sensitivity increases with an increase in the acetone concentration at the same operating temperature. At an operating temperature of 300 °C, the WO_3 nanoplate sensor has a sensitivity as high as 42 for a 1000 ppm acetone vapor, and it has a detectable limit as low as 2 ppm of acetone vapor with a sensitivity of about 4, as shown as curve A. At a low operating temperature of 100 °C, the sensitivities of the WO_3 nanoplate sensors are about 3 for 100–500 ppm acetone vapors (curve D in Fig. 37a). Figs. 37b-c show the response and recovery times of the WO_3 nanoplate sensors under various concentrations

of acetone vapors at operating temperatures of 250–300 °C. The response times of the WO_3 nanoplate sensors operating at 300 °C are 3–10 s in the vapor concentration range of 2–1000 ppm, and their corresponding recovery times are 6–13 s. For the case operating at 250 °C, the response times lie in a range of 8–15 s, and their recovery times are 15–31 s. Both the response times and recovery times increase with the increase in operating temperature.

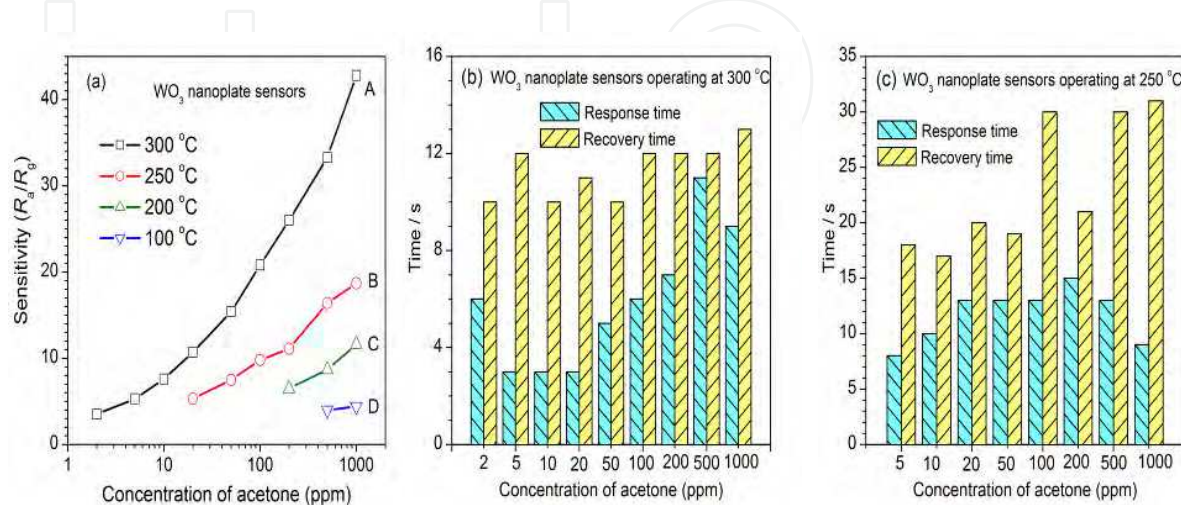


Fig. 37. (a) Sensitivities of the WO_3 nanoplate sensors as a function of the concentration of acetone vapor at various operating temperatures, and (b-c) response and recovery times of the WO_3 nanoplate sensors to acetone vapor with various concentrations operating at (b) 300 °C and (c) 250 °C. Reprinted with permission from *Sensor. Actuat. B-Chem.*, 2011, 153(2), 373–381. Copyright 2011 Elsevier.

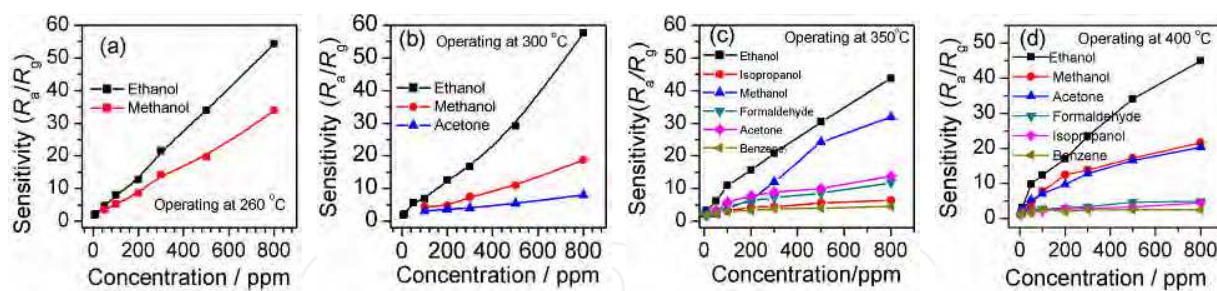


Fig. 38. The plots of the sensitivities of the $\alpha\text{-MoO}_3$ nanoplate sensors as a function of the concentrations of different reagent vapors operating at (a) 260 °C ($R_0 = 20 \text{ M}\Omega$), (b) 300 °C ($R_0 = 20 \text{ M}\Omega$), (c) 350 °C ($R_0 = 20 \text{ M}\Omega$), and (d) 400 °C ($R_0 = 4.7 \text{ M}\Omega$). Reprinted with permission from *J. Mater. Chem.*, 2011, 21(25), 9332–9342. Copyright 2011 Royal Society of Chemistry.

Fig. 38 shows the plots of the sensitivities of the $\alpha\text{-MoO}_3$ nanoplate sensors as a function of the concentrations of different reagent vapors operating at 260 – 400 °C. The sensitivities to ethanol vapors present a linearly increasing trend from 2 to 54 as the concentration of the ethanol vapor increases from 5 to 800 ppm, and a similar linear relationship is also seen for methanol vapors (4 – 34 for 50 – 800 ppm), when the operating temperature is 260 °C (Fig. 38a). When operated at 300 °C, the $\alpha\text{-MoO}_3$ nanoplate sensors show similar high sensitivities

to ethanol vapors (2 – 58 for 5 – 800 ppm), whereas their sensitivities to methanol vapors are 4 – 19 for 50 – 800 ppm, lower than those (4 – 34 for 50 – 800 ppm) operated at 260 °C, as shown in Fig. 38b. The sensitivities of the α -MoO₃ nanoplate sensors to acetone vapors shows a good linear increase with the increase in concentrations, but their sensitivities are less than 10 even at 800 ppm. For ethanol vapors, the sensitivities show a similar change trend when the operating temperature increases from 350 to 400 °C, and the sensitivity values increase from about 2 to 44 when the concentrations of ethanol vapors increase from 5 to 800 ppm. When the operating temperature is 400 °C, the sensitivities of isopropanol, formaldehyde and benzene vapors are very low (less than 5) in the concentration range of 5–800 ppm, whereas the sensitivities are about 1.2 – 22 for 5 – 800 ppm of methanol and acetone vapors.

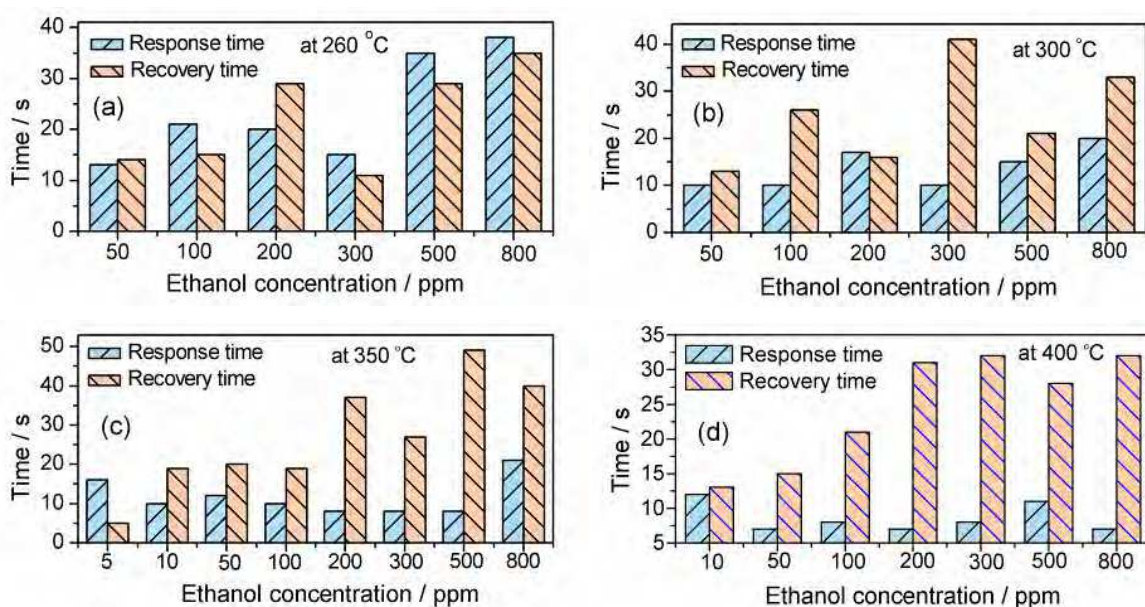


Fig. 39. The response and recovery times of the α -MoO₃ nanoplate sensors as a function of the ethanol concentrations operating at 400 °C ($R_0 = 4.7 \text{ M}\Omega$). Reprinted with permission from *J. Mater. Chem.*, 2011, 21(25), 9332–9342. Copyright 2011 Royal Society of Chemistry.

Fig. 39 shows the response and recovery times of the α -MoO₃ nanoplate sensors to ethanol vapors with various concentrations. Generally, the response times of α -MoO₃ nanoplate sensor decrease with the increase in operating temperature, from 15 – 38 s at 260 °C to 7 – 14 s at 400 °C. However, the recovery times (i.e., 10 – 40 s) almost show no obviously change in the operating temperature range of 260 – 400 °C. The recovery time slightly increases with an increase in the concentration of ethanol vapors (Figs. 39c-d).

The space-charge layer model has often been applied to explain the possible gas-sensing mechanism of a semiconducting metal oxide sensor. WO₃ and MoO₃ are typical *n*-type metal oxide semiconductors, and the space-charge layer model is suitable to WO₃ and MoO₃ nanoplate sensors. When the nanoplate sensor is exposed to air, O₂ molecules will adsorb on the surfaces of WO₃ nanoplates. The O₂ molecules adsorbed then transform to be oxygen ions (e.g., O[−], O^{2−}, or O₂[−]) by capturing free electrons from the conductance band of nanoplates. The electron-capture process leads to a depletion region in semiconductor nanoplates, which reduces the conductive regions, and thus a high-

resistance state is formed, as shown in Fig. 40a. When the nanoplate sensors are exposed to reducing gases (i.e., alcohol, and acetone vapors), the molecules adsorbed on the surfaces of the semiconductor nanoplates can provide electrons to reduce oxygen ions, and then release free electrons back into nanoplates. This process decreases the depletion region and form a conducting channel, which results in a low-resistance state, as shown in Fig. 40b.

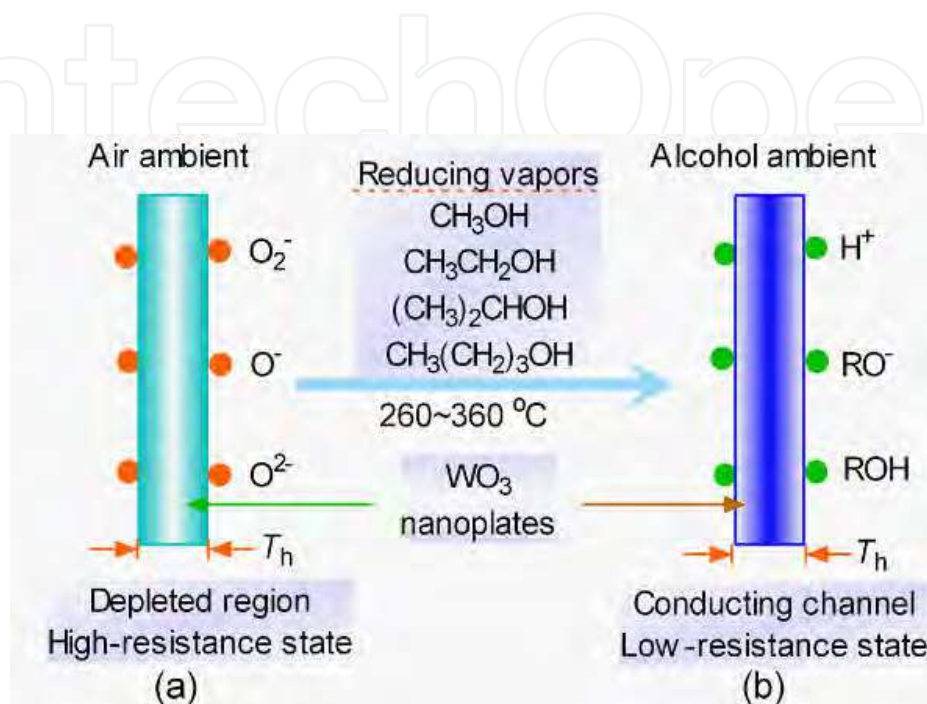


Fig. 40. A schematic representation of the alcohol sensing mechanism for WO_3 nanoplate sensors. Reprinted with permission from *Nanotechnology*, 2010, 21, 035501. Copyright 2010 IOP Publishing Ltd.

The sizes and shapes of the semiconductor nanocrystals, together with their configuration, are the key factors influencing the gas-sensing properties. Reducing the sizes of the active materials down to several nanometers can enhance the gas-sensing performance. However, the particles with nanoscale sizes tend to form aggregates, as shown in Fig. 41c. The long diffusion length and the sluggish diffusion of a target gas into the inner parts of the secondary aggregates is inefficient to improve the gas-sensing property. Only the resistance of the primary nanoparticles near the surfaces of the aggregates is affected by the target gas molecules, and thus the sensitivity is low and the response time is long, as shown in Fig. 41d. But for the ultrathin 2D nanoplates, they usually form a loose assembly containing a great number of gaps due to the steric effect of the platelike morphology, as shown in Fig. 41a. The gaps between nanoplates not only enhance the effective surface to adsorb target gases, but also provide capacious channels for target gases to diffuse. The large surface areas for the effective adsorption and the loosely assembling structures for the rapid diffusion of target gases are helpful to enhance the sensitivities and shorten the response times of the 2D nanoplate sensors (Fig. 41b).

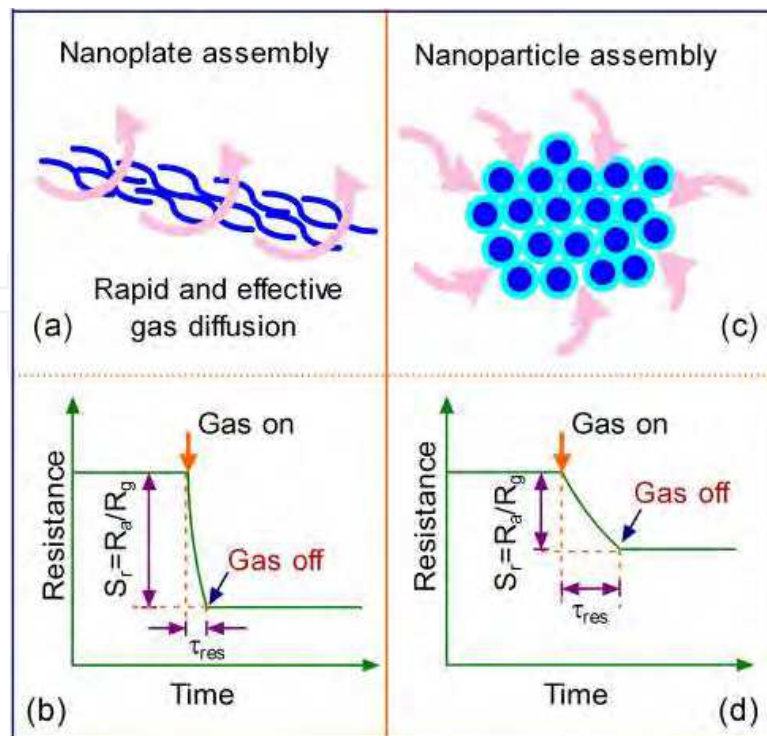


Fig. 41. A schematic representation of the configuration effect of the semiconductor nanoplates and nanoparticles on their alcohol sensing performance. Reprinted with permission from *Nanotechnology*, 2010, 21, 035501. Copyright 2010 IOP Publishing Ltd.

8. Conclusions

Topochemical conversion of inorganic-organic hybrid compounds into low-dimensional inorganic nanostructures is an efficient strategy to achieve advanced functional materials with smart control in crystal size and shape. The inorganic-organic hybrid compounds can be synthesized via intercalation chemical reactions between layered inorganic host solids and suitable organic guest molecules. The nanostructures obtained by this topochemical conversion route usually inherit the morphologies and sizes of their corresponding hybrid precursors, and using this method one can readily synthesize some special low-dimensional materials, e.g. carbides and nitrides. The outstanding advantages of the topochemical conversion route are the ready control in dimensions and the ability of cost-effective and large-scale synthesis. The as-obtained nanocrystals can have wide applications in photocatalysts, sensors, and energy conversion.

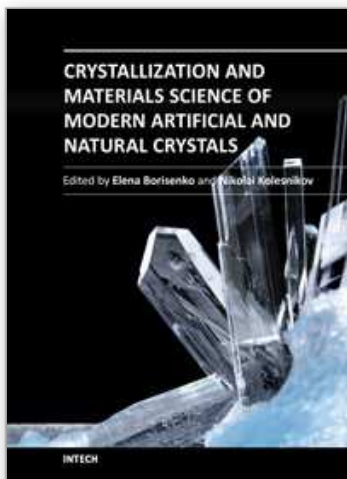
9. Acknowledgment

This work was supported by the National Natural Science Foundation of China (Grant No. 50802090, 51172211), the China Postdoctoral Science Foundation (Grant No. 20090450094, Grant No. 201003397), the Opening Project of State Key Laboratory of High Performance Ceramics and Superfine Microstructure (Grant No. SKL200905SIC), and the Young Scientist Exchange Program between the Republic of Korea and the People's Republic of China. The author thanks Prof. Yoshiyuki Sugahara (Waseda University) for his valuable discussion in the formation mechanism of tungstate-based inorganic-organic hybrid compounds. The

author also thanks Prof. Lian Gao, Prof. Rui Zhang, Prof. Jing Sun, Prof. Xinjian Li, Prof. Hongxia Lu, Prof. Hongliang Xu, Prof. Daoyuan Yang, Prof. Hailong Wang, Dr. Bingbing Fan, Mr. Hejing Wen, Mr. Xianxiang Hou, Ms Zhongsheng Liu, Ms Li Yin, Mr. Tao Li, Ms Mina Liu, Mr. Yi Zhang and Mr. Haitao Zhai for their kind help in some of the experiments.

10. References

- [1] D. L. Chen and Y. Sugahara, Tungstate-based inorganic-organic hybrid nanobelts/nanotubes with lamellar mesostructures: synthesis, characterization, and formation mechanism. *Chem. Mater.*, 2007, 19(7), 1808-1815.
- [2] D. L. Chen, and Y. Sugahara, Investigation of factors influencing the formation of tungstate-based inorganic-organic hybrid nanobelts/nanotubes. *Key Eng. Mater.*, 2007, 352, 85-88.
- [3] D. L. Chen, H. L. Wang, R. Zhang, S. K. Guan, H. X. Lu, H. L. Xu, D. Y. Yang, Y. Sugahara and L. Gao, Synthesis, characterization and formation mechanism of single-crystal WO_3 nanosheets via an intercalation-chemistry-based route. *Chem. J. Chinese U.*, 2008, 29(7), 1325-1330.
- [4] D. L. Chen, T. Li, L. Yin, X. Hou, X. Yu, Y. Zhang, B. Fan, H. Wang, X. Li, R. Zhang, T. Hou, H. Lu, H. Xu, J. Sun and L. Gao, A comparative study on reactions of n-alkylamines with tungstic acids with various W-O octahedral layers: Novel evidence for the "dissolution-reorganization" mechanism. *Mater. Chem. Phys.*, 2011, 125(3), 838-845.
- [5] D. L. Chen, H. L. Wang, R. Zhang, L. Gao, Y. Sugahara and A. Yasumori, Single-crystalline tungsten oxide nanoplates. *J. Ceram. Process. Res.*, 2008, 9(6), 596-600.
- [6] D. L. Chen, L. Gao, A. Yasumori, K. Kuroda and Y. Sugahara, Size- and shape-controlled conversion of tungstate-based inorganic-organic hybrid belts to WO_3 nanoplates with high specific surface areas. *Small*, 2008, 4(10), 1813-1822.
- [7] D. L. Chen, M. Liu, L. Yin, T. Li, Z. Yang, X. Li, B. Fan, H. Wang, R. Zhang, Z. Li, H. Xu, H. Lu, D. Yang, J. Sun and L. Gao, Single-crystalline MoO_3 nanoplates: topochemical synthesis and enhanced ethanol-sensing performance. *J. Mater. Chem.*, 2011, 21(25), 9332-9342.
- [8] D. L. Chen, H. Wen, T. Li, L. Yin, B. Fan, H. Wang, R. Zhang, X. Li, H. Xu, H. Lu, D. Yang, J. Sun and L. Gao, Novel pseudo-morphotactic synthesis and characterization of tungsten nitride nanoplates. *J. Solid State Chem.*, 2011, 184(2), 455-462.
- [9] D. L. Chen, H. Wen, H. Zhai, H. Wang, X. Li, R. Zhang, J. Sun and L. Gao, Novel synthesis of hierarchical tungsten carbide micro-/nanocrystals from a single-source precursor. *J. Am. Ceram. Soc.*, 2010, 93(12), 3997-4000.
- [10] D. L. Chen, X. Hou, H. Wen, Y. Wang, H. Wang, X. Li, R. Zhang, H. Lu, H. Xu, S. Guan, J. Sun and L. Gao, The enhanced alcohol-sensing response of ultrathin WO_3 nanoplates. *Nanotechnology*, 2010, 21, 035501.
- [11] D. L. Chen, X. Hou, T. Li, L. Yin, B. Fan, H. Wang, X. Li, H. Xu, H. Lu, R. Zhang and J. Sun, Effects of morphologies on acetone-sensing properties of tungsten trioxide nanocrystals. *Sensor. Actuat. B Chem.*, 2011, 153(2), 373-381.



Crystallization and Materials Science of Modern Artificial and Natural Crystals

Edited by Dr. Elena Borisenko

ISBN 978-953-307-608-9

Hard cover, 328 pages

Publisher InTech

Published online 20, January, 2012

Published in print edition January, 2012

Crystal growth is an important process, which forms the basis for a wide variety of natural phenomena and engineering developments. This book provides a unique opportunity for a reader to gain knowledge about various aspects of crystal growth from advanced inorganic materials to inorganic/organic composites, it unravels some problems of molecular crystallizations and shows advances in growth of pharmaceutical crystals, it tells about biomineralization of mollusks and cryoprotection of living cells, it gives a chance to learn about statistics of chiral asymmetry in crystal structure.

How to reference

In order to correctly reference this scholarly work, feel free to copy and paste the following:

Deliang Chen (2012). Topochemical Conversion of Inorganic–Organic Hybrid Compounds into Low-Dimensional Inorganic Nanostructures with Smart Control in Crystal-Sizes and Shapes, Crystallization and Materials Science of Modern Artificial and Natural Crystals, Dr. Elena Borisenko (Ed.), ISBN: 978-953-307-608-9, InTech, Available from: <http://www.intechopen.com/books/crystallization-and-materials-science-of-modern-artificial-and-natural-crystals/topochemical-conversion-of-inorganic-organic-hybrid-compounds-into-low-dimensional-inorganic-nanostr>

INTECH
open science | open minds

InTech Europe

University Campus STeP Ri
Slavka Krautzeka 83/A
51000 Rijeka, Croatia
Phone: +385 (51) 770 447
Fax: +385 (51) 686 166
www.intechopen.com

InTech China

Unit 405, Office Block, Hotel Equatorial Shanghai
No.65, Yan An Road (West), Shanghai, 200040, China
中国上海市延安西路65号上海国际贵都大酒店办公楼405单元
Phone: +86-21-62489820
Fax: +86-21-62489821

© 2012 The Author(s). Licensee IntechOpen. This is an open access article distributed under the terms of the [Creative Commons Attribution 3.0 License](#), which permits unrestricted use, distribution, and reproduction in any medium, provided the original work is properly cited.

IntechOpen

IntechOpen